Dynamical Interpolation and Forecast of the Evolution of Mesoscale Features off Northern California

MICHELE M. RIENECKER[1] AND CHRISTOPHER N. K. MOOERS[1]

Dept. of Oceanography, Naval Postgraduate School, Monterey, CA 93943

ALLAN R. ROBINSON

Center for Earth and Planetary Physics, Harvard University, Cambridge, MA 02138

(Manuscript received 11 September 1986, in final form 14 January 1987)

ABSTRACT

The series of cruises off Northern California comprising OPTOMA11, during two months in summer 1984, were specifically designed as an ocean prediction experiment. In addition to a regional survey from Cape Mendocino to Monterey, six surveys were made of a (150 km)^2 domain offshore of Pt. Arena/Pt. Reyes. During the initial phase (over about ten days) of OPTOMA11, an intense (speeds up to 50 cm s^{-1}, relative to 450 m) jet/cyclone system propagated offshore at about 5 km day^{-1}. The subsequent evolution (over about 40 days) of the streamfunction field was governed by the meandering of the jet and the associated changes in the intensity of the anticyclonic region to the north of the jet and the cyclonic region to the south. From quasi-geostrophic (QG) model hindcast experiments using the streamfunction data, wind stress curl was an important forcing mechanism in the later phase of the experiment. Forecasts in a domain extending over the continental slope were in agreement with objective analyses (OA) in the upper water column when the local topographic slope was used in the model. Asynopticity in initialization data (in this case, data acquired over eight days) did not seriously degrade forecasts, although forecasts which used synoptic estimates (via a time-dependent objective analysis) of initial and boundary data were more accurate. The repetition in sampling allowed estimation of a space–time covariance function which was used for statistical forecasts. Quasi-geostrophic dynamical forecasts, generated using statistically forecast boundary data, evolved consistent with the OA in the interior of the forecast domain (rms difference 56% after 16 days). Assimilation of truly synoptic data, in the interior of the forecast domain as well as on the boundaries, improved the forecast so that it gave a better estimate of the streamfunction field than the OA (rms difference from the best field estimate was 20% after 16 days). Energetics analyses, based on best estimates of the streamfunction and vorticity fields obtained by dynamical interpolation, indicate that the cyclonic region to the south of the jet grew due to baroclinic instability. The inclusion of wind stress curl forcing was essential to the interpretation of the energetics.

1. Introduction

Prediction of the evolution of ocean synoptic/mesoscale phenomena (e.g., eddies, meandering jets, fronts) has been attempted only over the last few years as the number of well-resolved observations of such phenomena has increased and an understanding thus gained of their role in the ocean circulation, mixing, transport of heat, nutrients, etc. (e.g., Robinson, 1983). The results of one of the earliest forecast experiments, using a periodic, quasi-geostrophic (QG) model and MODE data (McWilliams and Shen, 1980), were limited by the use of artificial boundary conditions necessarily imposed because of inadequate information to define the interaction between the ocean exterior to the forecast domain and the forecast ocean. More recent ocean forecast experiments have included simulations to investigate the importance of boundary updating and the identification of error accumulation in limited-area, open ocean, QG models (Robinson and Haidvogel, 1980; Miller et al., 1983). Hindcast experiments (i.e., dynamical interpolation rather than dynamical extrapolation) using real ocean data (e.g., Robinson et al., 1986) have produced dynamically interpolated fields for energy and vorticity analyses of the interactions and evolution of mesoscale features.

The goals of the OPTOMA (Ocean Prediction Through Observation, Modeling, and Analysis) Program include determining the capabilities and limitations of methodologies for real-time, continually operating observing and forecasting systems in a limited-area, open ocean domain. The ocean descriptive–predictive system (ODPS) for four-dimensional data assimilation which is being developed relies on an observing system and both statistical and dynamical models (Robinson and Leslie, 1985). OPTOMA's first

[1] Present affiliation: Institute for Naval Oceanography, NSTL, MS 39529.

pilot ocean prediction experiment, OPTOMA5 (Robinson et al., 1986), was conducted in summer 1983 in the California Current System (CCS). In the associated hindcast experiments, it was found that the evolution of mesoscale features in the CCS could be usefully forecast over two-week periods if sufficiently accurate, updated boundary data were available.

The OPTOMA11 experiment, in summer 1984, was conducted in roughly the same region off the coast of northern California as for OPTOMA5. It provided adequate information for several initialization and verification fields for dynamical model interpolation (hindcast) experiments in a (150 km)^2 domain. The duration of the experiment and the use of two research ships and, on one occasion, an aircraft, allowed the estimation of a time-dependent covariance function, so that synoptic estimates of the fields could be made as well as statistical *forecasts* by statistical objective analysis (OA). For the OPTOMA5 experiment, which consisted of three surveys about two weeks apart, the asynoptic data from each survey [covering a (120 km)^2 domain in about four days] were used as if synoptic.

This paper describes the evolution of streamfunction (or dynamic height) fields over the duration of the experiment. Examples are given of OPTOMA's present methodology for assimilating initial and boundary data into numerical experiments which hindcast or forecast the evolution of the QG streamfunction for periods of about two weeks. *Hindcasts,* where data acquired through to the end of the model integration period are used to estimate boundary data during the integration (these were termed "forecast experiments" by Robinson et al., 1986), allow a dynamically consistent description of the evolution of the fields over the entire experiment. In *dynamical forecasts,* boundary data are supplied through *statistical forecast* or extrapolation from the initialization field.

Since the near-bottom flow is weak in the model integration experiments here, the inclusion of the continental slope is possible; hindcasts are improved when the local topographic slope is used instead of a flat bottom ocean. During the initial phase of OPTOMA11, surface dynamic height (SDH) patterns were well-correlated with sea surface temperature (SST) patterns. This relationship is exploited to carry out dynamical interpolation for short periods using satellite-derived SST. As for OPTOMA5, best estimates of streamfunction and vorticity fields are formed by assimilating forward and backward dynamical interpolation fields. Energetics analyses are carried out with these dynamically filtered fields. During OPTOMA5, the limited-area flow regime was very different from that encountered during OPTOMA11 in that eddies, their merger (due to barotropic instability) and subsequent evolution dominated the variability. During OPTOMA11, the meandering jet dominates the flow over the entire experiment and there is evidence for cyclone intensification to the south of the jet through baroclinic instability. In addition, wind stress curl is an important forcing mechanism during part of OPTOMA11.

2. The OPTOMA11 experiment

The first major OPTOMA ocean prediction experiment, OPTOMA11, was conducted in June and July 1984. Most of the data acquisition (primarily XBT and CTD casts to about 500 m) was concentrated in a (150 km)^2 domain centered approximately 180 km offshore of Pt. Arena (offshore of the site of the Coastal Ocean Dynamics Experiment), Fig. 1. The size of the domain was limited because of the desire for quasi-synoptic realizations of the mass field, but was large enough (about six times the internal Rossby radius of deformation) that several synoptic/mesoscale features would likely be encountered. In the design of the observing system, emphasis was placed on the acquisition of boundary data around submodules of the order of (75 km)^2, with data acquired in the interior of these modules as time permitted. The primary experimental domain, termed "module 0," consisting of the union of these submodules to form the (150 km)^2 region, was sampled six times during two months. The design goal for the primary mappings was to cover the entire domain for the initialization of the dynamical model or verification of its forecasts. Subsequently, the goal was to acquire additional boundary data and to expand the data acquisition domain especially over the continental slope, since, from previous OPTOMA mappings, the

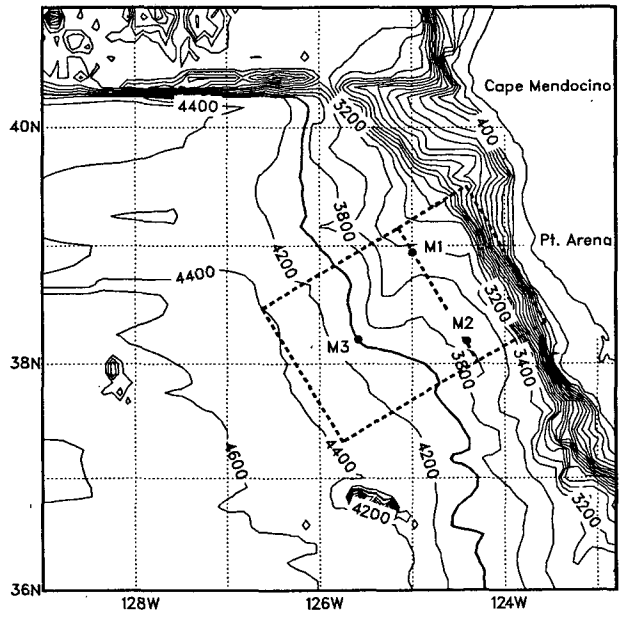

FIG. 1. The domains used for the dynamical interpolation experiments of OPTOMA11. The square (dashed) box offshore is the primary domain. For some experiments, this domain was extended over the continental slope as shown. The location of current meter moorings are shown by solid circles. The bathymetry is given in meters.

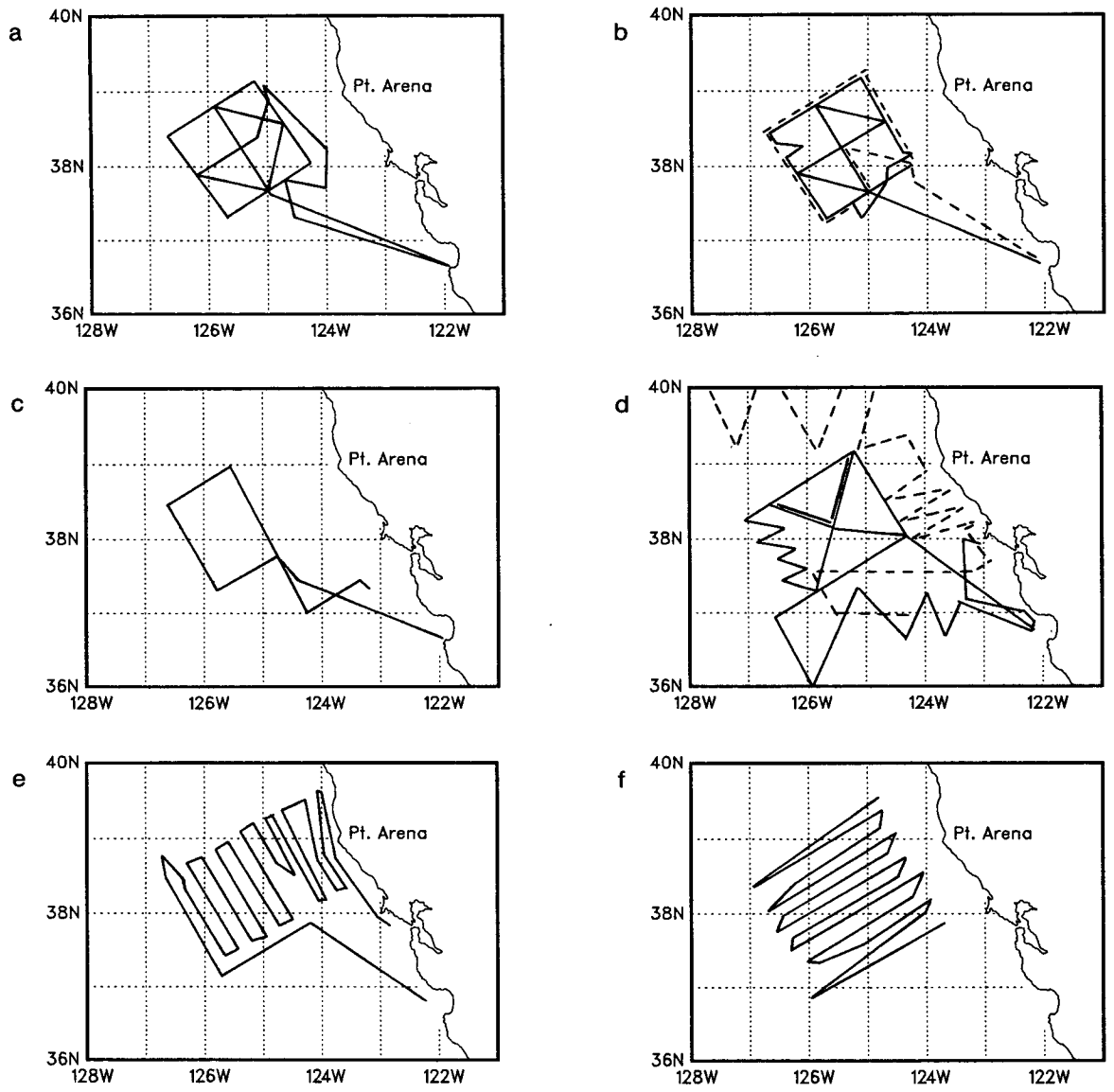

FIG. 2. Cruise tracks for OPTOMA11: (a) AI: 5–15 June; (b) AII: 21–30 June; (c) AIII: 5–13 July; (d) DI: 23–30 June (dashed line) and DII: 30 June–10 July (solid line); (e) DIII: 27 July–5 August; (f) P: 18 July.

most energetic boundary forcing was likely to be on the inshore boundary. Additional data would also be acquired farther offshore, for clarification of feature evolution. In addition to the five quasi-synoptic shipborne mappings, one fully synoptic AXBT mapping was carried out by a U.S. Navy P3 aircraft on 18 July. The use of two research ships, the R/V *Acania* and the USNS *de Steiguer,* also allowed one, albeit asynoptic, regional mapping from Cape Mendocino to Monterey; this enabled the features in the smaller domain to be related to the external domain and to features in satellite IR imagery.

The individual cruise components and the number and type of casts acquired are summarized in Table 1; the cruise tracks are shown in Fig. 2. Station spacing along tracks was typically 18 km. Temperature profiles were mainly acquired by XBT because of the desire for rapid transit over the domain. The average $S(T)$ profile determined from CTDs during the cruise period was used to convert XBT temperature profiles to density profiles needed for estimating the quasi-geostrophic streamfunction. This procedure is most subject to error in the upper 100 m, where the $S(T)$ relation is not tight, and over the continental shelf and slope where a change in the $S(T)$ relation may be expected. The associated root-mean-square error in the surface dynamic height is estimated to be about 2 dyn cm (estimated using the mean $S(T)$ relation in calculating dynamic height at CTD stations instead of the in situ salinity). This error is to be compared with a typical

TABLE 1. Summary of data recovered during OPTOMA11.

Leg	Period (1984)	AXBT	XBT	CTD	Central day*
AI	5–15 Jun	—	103	31	161
AII	21–30 Jun	—	145	21	177
AIII	5–13 Jul	—	61	1	191
DI	23–30 Jun	—	99	28	—
DII	30 Jun–10 Jul	—	121	28	187
DIII	27 Jul–5 Aug	—	152	27	215
P	18 Jul	62	—	—	200

* As pertains to module 0.

dynamic range of 20 dyn cm over the OPTOMA11 domain.

Although the primary OPTOMA11 domain was located in deep water (average depth about 4000 m), over very gently sloping bathymetry, its mesoscale features interact with coastal topography and circulation and are also possibly influenced by the Mendocino Escarpment. From the OPTOMA database, eddies (with various scales) and meandering current filaments are present year round. During summer, the mesoscale features in the OPTOMA domain are either directly related to or influenced by the coastal upwelling jet forced by the generally equatorward winds. Cool filaments often extend far offshore from their coastal source, especially between Pt. Reyes and Pt. Arena, but also from Cape Mendocino (and other prominent points along the coast). These features have been noted on previous OPTOMA cruises (e.g., Mooers and Robinson, 1984; Rienecker et al., 1985), on surveys described by Kosro and Huyer (1986) and also in satellite imagery (e.g., Kelly, 1983).

3. The objectively analyzed fields

a. Asynoptic fields

The regional maps of SST and SDH relative to 450 m, Fig. 3, were acquired from 23 June to 10 July. Synoptic AVHRR images, from the NOAA-7 polar orbiting satellite, for 20 and 30 June are shown for comparison, Fig. 4. These maps show typical summertime features for this area: cool, cyclonic coastal upwelling centers off Cape Mendocino and Pt. Reyes/Pt. Arena; an offshore jet, embedded in a cool anomaly, with geostrophically estimated speeds of up to 40 cm s^{-1}, relative to 450 m; a larger scale (diameter about 150 km) anticyclone to the north of the jet and a narrow cyclonic shear zone [a band of smaller scale (diameter about 50 km) cyclones, e.g., Fig. 6] to the south of the jet. The jet bifurcated far offshore and was either partially entrained into the anticyclone or meandered off to the south. The exact details vary from year to year, but this general scenario was also encountered during the OPTOMA5 experiment in 1983. The changes in the IR images, Fig. 4, give an indication of the degree of asynopticity in the regional maps. Between 20 and 30 June, the offshore extremity of the cool anomaly extended about 60 km farther offshore and the northern boundary of the offshore portion of the anomaly moved about 20 km farther south. The cool anomaly narrowed and several small cyclones developed in the cyclonic shear zone to the south of the anomaly. Some cool filaments evident to the south of the major anomaly on 20 June substantially "retreated" by 30 June. Based on imagery not shown, these trends, with a subsequent decay of the cyclones and a sharpening of the SST front on the southern side of the anomaly, continued to 6 July.

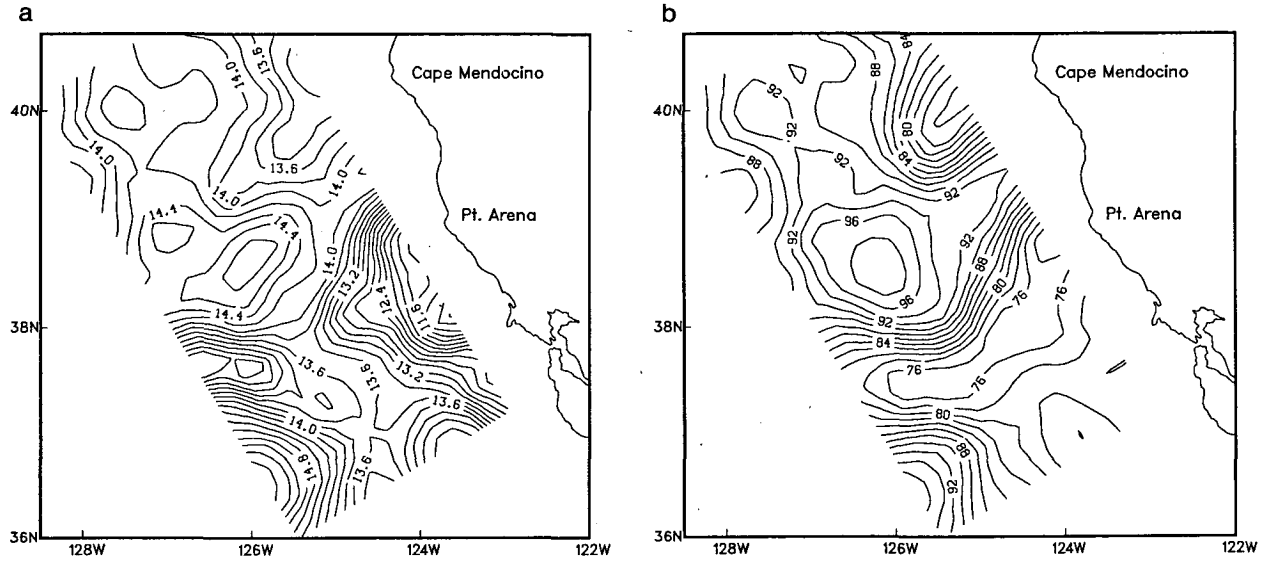

FIG. 3. Quasi-synoptic maps from DI and DII, 23 June to 10 July 1984. (a) SST; (b) SDH, relative to 450 m.

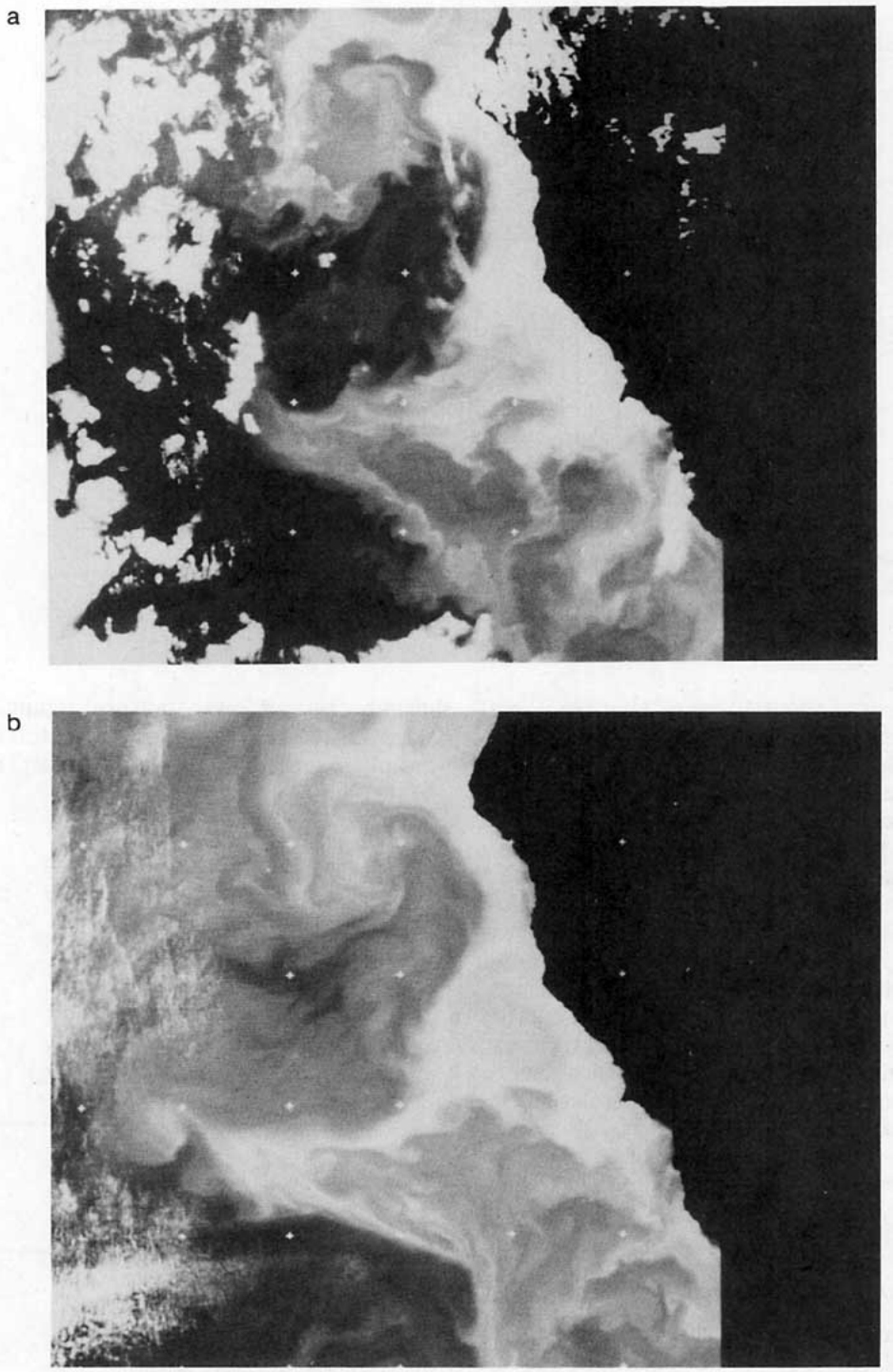

FIG. 4. AVHRR image (Channel 4) (with a 1° × 1° latitude/longitude grid superposed), from the NOAA7 satellite: (a) 20 June 1984, (b) 30 June 1984.

From the series of SDH maps in the primary domain (centered at 38°15′N, 125°27′W, with the y-axis oriented 38° W of N), Fig. 5, the initial (5 to 15 June) intense jet/cyclone system in the southern part of the domain, with maximum speeds of about 50 cm s^{-1}, propagated offshore. For AII and subsequent maps, the meandering jet dominated the fields. The jet was surface intensified, with speeds of up to 60 cm s^{-1}, and extended to a depth of at least 200 m. By late July–early August, the jet speeds had decreased somewhat

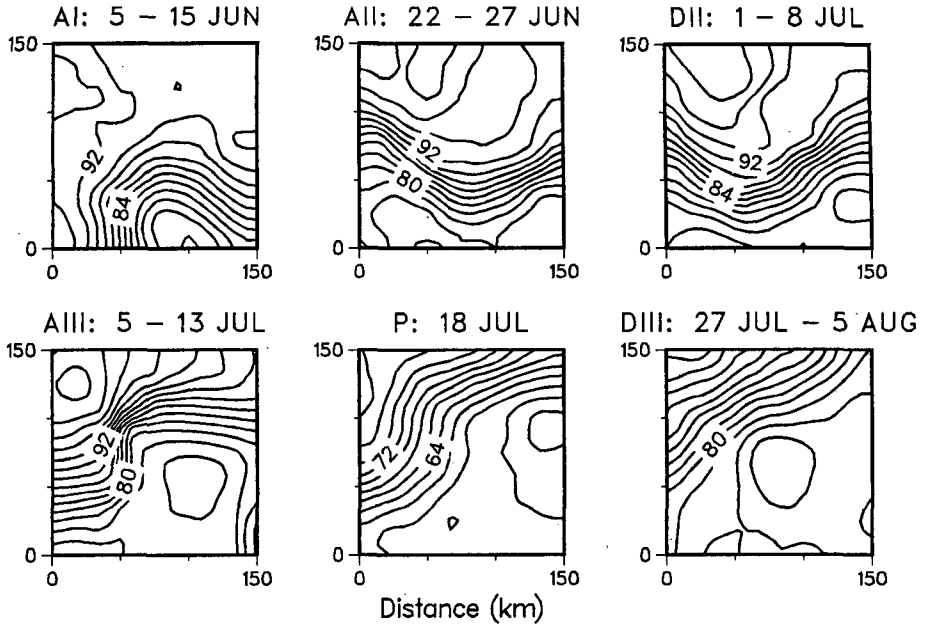

FIG. 5. SDH, relative to 450 m (except for P, where a 300 m reference level is used), from the cruises covering module 0.

(maximum speeds of about 40 cm s^{-1}) but the jet had broadened so that the transport was not much diminished. (The offshore transport of the jet over the upper 300 m is estimated to be about 2 Sv; most of this is confined to the upper 100 m.) The anticyclonic feature to the north of the jet propagated out of the domain and as the jet moved farther north in the eastern part of the domain, the region of cyclonic flow broadened.

The two maps of surface dynamic height in the extended domain, Fig. 6, show the offshore, northward movement of the jet close to the coast, the offshore propagation of the cyclones south of the jet, and the persistence of northward flow in the southeast corner. This apparent alongshore convergence, which may be important in the maintenance (and perhaps even generation) of the offshore flowing jet, was also evident farther offshore in current meter data (see Fig. 1 for mooring locations) acquired by R. L. Smith at Oregon State University, in association with OPTOMA, in summer 1985 (Rienecker et al., 1987).

b. *The statistical interpolation method*

The data from approximately 800 stations acquired during OPTOMA11 were used to determine the anisotropic, space–time covariance function, Fig. 7, which was calculated from surface dynamic height data in 15 km by 15 km by 5 day bins. At zero time-lag, the fields are nearly isotropic for distance-lags up to about 50 km. The predominant time variation of the covariance function, inferred from Fig. 7, is consistent with a westward phase propagation at about 5 km day^{-1}. The covariance function at a central lag of ten days (calculated from data at lags from 7.5 to 12.5 days) is not shown because of lower statistical significance (fewer data points being used in the calculation). The westward phase propagation was still (barely) evident, but

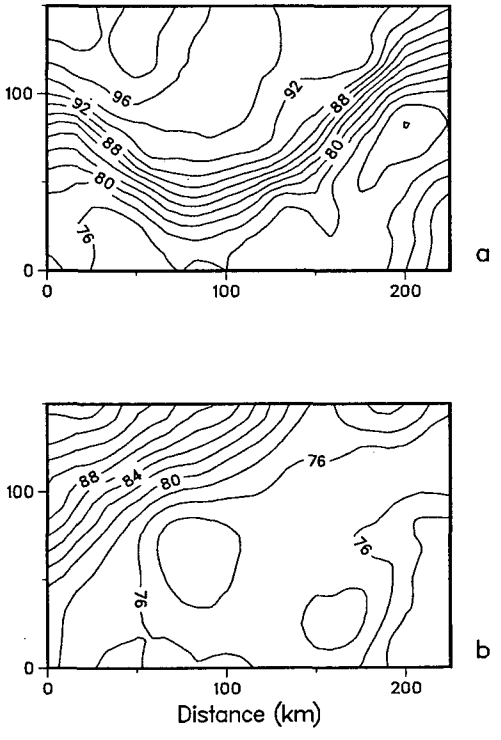

FIG. 6. SDH, relative to 450 m, from (a) AII and DI, 23 to 29 June 1984; (b) DIII, 27 July to 5 August 1984.

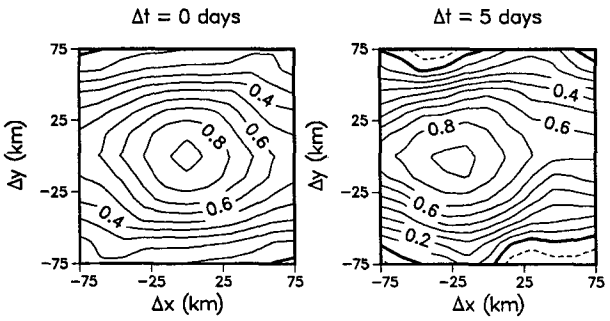

FIG. 7. The space–time covariance function estimated from SDH.

a confident estimate of a phase speed could not be made. The isotropic function

$$C(r) = C_0[1 - (r/a)^2]e^{-(r/b)^2}$$

(where $r = |\mathbf{x} - \mathbf{c}t|$, $c = 5$ km day^{-1} westward) was fit to the isotropic covariance function estimated from the data. The calculated covariance at zero-lag is the sum of the mesoscale signal variance, C_0, and the noise variance, ϵ, which is due to submesoscale processes as well as instrument noise (and "noise" associated with the use of a mean $S(T)$ relation with the XBT profiles and with noise at the assumed reference level). No estimate can be made of the covariance function associated with the submesoscale processes because of the relatively coarse station spacing; hence, it is assumed that this covariance is nonzero only at the zero-lag. This assumption is acceptable if the station spacing is comparable to or larger than the analysis grid (Clancy, 1983), as is the case for this study. An estimate of ϵ, and also of C_0 is made by extrapolating the function $C(r)$, fit to the calculated covariance at nonzero lags, to $r = 0$. The covariance is then normalized by C_0. The OA uses $C(r)$, for $r \neq 0$, and $C(0) = 1 + \epsilon$, where ϵ is now the ratio of noise to signal variance. From the OPTOMA11 data, $\epsilon = 0.1$, $a = 79$ km and $b = 102$ km. This covariance function, with the time dependence included simply as the phase propagation noted above, was used in the statistical OA model (e.g., Bretherton et al., 1976) to produce synoptic estimates of the nondimensional streamfunction field (with error estimates) at two-day (when possible) intervals, on a $(150 \text{ km})^2$ grid with grid spacing 8.3 km, for dynamical model initialization and verification. The streamfunction fields, e.g., Fig. 11, were calculated by limiting the number of influence points used in the objective analysis to five. The initial spatial and temporal radii of influence were 50 km and six days, although these limits were expanded, up to 100 km and 10 days, if only two, or fewer, data points were found within the initial limits.

c. *The vertical extension process*

The mass field data acquired during OPTOMA11 do not permit estimation of the barotropic flow component. As for the OPTOMA5 experiment (Robinson et al., 1986), this deficiency is compensated for in a simplified manner by assuming a constant reference level throughout the domain over the entire forecast period. The reference level is chosen, by trial and error, to give the "best" forecast at all levels. In addition to the problem of using a reference level that may be below the common maximum depth (450 m) of most data, the streamfunction must be estimated at the deeper levels of the dynamical model. (Here, the streamfunction at 50, 150, 400, 1070, 2150 and 3380 m, for an average ocean depth of 4000 m, is used for the model.) These estimates are formed by a vertical extension process which uses the eofs (empirical orthogonal functions) of density determined from the deep (3000 m) casts acquired during the experiment to extrapolate the shallow profiles to the bottom.

From the eleven deep CTD casts, the first full profile (3000 m) density eof, Fig. 8a, explains 91% of the full water column variance. The fraction of variance explained by the eof at any depth depends on the component of the eof at that depth as well as the eigenvalue. The first eof explains 75% of the variance at the surface; 96% at 150 m; 87% at 400 m; 71% at 760 m; 47% at 1000 m; 4% at 2000 m. At depth, more variance is explained by the (noisier) higher eofs. To estimate the density anomaly at the lower levels of the dynamical model from shallow casts and the full profile eofs requires a least-squares fit. The similarity of the first two eofs below about 60 m makes it difficult to estimate the amplitude of more than the first eof. These problems may be slightly alleviated by using eofs for subprofiles (0 to 300, 310 to 450, 460 to 750 and 760 to 3000 m). The subprofile boundaries are defined by the depth of various types of casts, e.g., AXBTs sampled only the upper 300 m. In the deepest section (760 to 3000 m) the first eof explains 79% of the total variance. This eof explains 88% of the variance at 760 m; 96% at 1000 m; 38% at 2000 m. Below about 1500 m, the first two eofs explain about 70% of the variance. The first two full profile and subprofile eofs, Fig. 8, account for most of the variance, Table 2. The eofs from the eleven OPTOMA11 profiles were not substantially changed by incorporation of more (up to 28) profiles from cruises in summer 1985. The stability, and representativeness, of the eofs in the upper 300 m, calculated from only 11 profiles, is remarkable, as shown by a comparison with eofs calculated from 460 shallow profiles in module 0, Fig. 8c. The principal components of each subprofile were regressed onto the principal components of the full profile eofs (see appendix A). In this way, the signal in the upper water column was used to estimate, by regression analysis, the signal below. The regression analysis was limited to two eofs for each subprofile and two for the full profile. The integral of the estimated density anomaly, with appropriate multiplicative factors, yields the nondimensional streamfunction. (To obtain the streamfunction at 3380

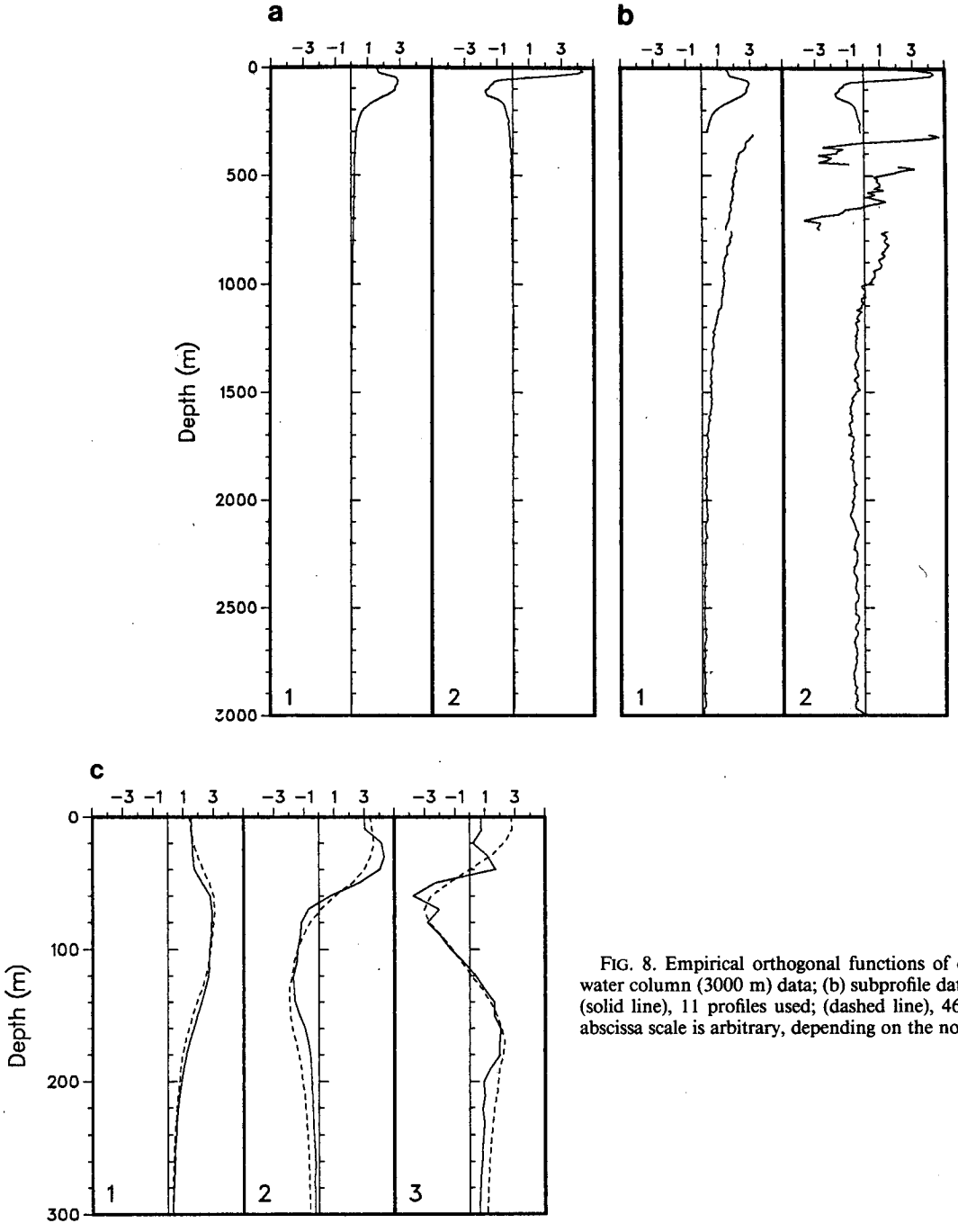

FIG. 8. Empirical orthogonal functions of density from (a) full water column (3000 m) data; (b) subprofile data; (c) data to 300 m: (solid line), 11 profiles used; (dashed line), 460 profiles used. The abscissa scale is arbitrary, depending on the normalization factor.

m, the density anomaly was assumed to be constant from 3000 m to the bottom.)

The vertical extension process was verified, using CTDs, by calculating the streamfunction, relative to 750 m, from profiles estimated by regression below 300 m and comparing the result with the streamfunction determined from the "raw" profiles. From 116 profiles to 750 m, the mean square difference was equivalent to 0.4% of the data variance at 50 m, to 2% at 150 m, and to 15% at 400 m. Below 750 m, the errors can only be estimated from the 11 profiles used for the regression analysis. If all eofs are used in the regression, the error is zero. If fewer eofs are used, the errors are due to the truncation (in the basis function expansion) and to the uncertainty in the regression estimates. From these 11 profiles, the error is less than 4% in the upper water column and is 21% at 1070 m, 43% at 2150 m, and 56% at 3380 m.

The nondimensional streamfunction profiles were calculated from the integral of the first two full profile

TABLE 2. Percent variance explained by each EOF.

	EOF				
Section	1	2	3	4	5
0–3000 m	90.6	7.0	1.3	0.4	0.3
0–300 m	91.1	7.1	1.0	0.4	0.2
310–450 m	99.2	0.5	0.5	0.1	0.1
460–750 m	98.2	0.8	0.5	0.1	0.1
760–3000 m	78.9	14.0	2.1	1.8	1.0

eofs (using a reference level of 3000 m), Fig. 9. The first eof yields a profile very much like a first baroclinic dynamical mode, with the zero crossing shifted by a barotropic component. The second mode is much more surface-trapped than the corresponding dynamical mode. The first mode, which explains most of the variance, has very little shear below 1000 m; hence reference levels chosen below that will be essentially equivalent and will correspond to lower layers almost at rest compared to the much more energetic upper layers. A 750 m reference level was used for the model integration experiments here. The streamfunction variance at the levels of the model, normalized by the variance at 150 m, is in reasonable agreement with the variance calculated from velocity time series at current meter moorings in the OPTOMA domain, Fig. 10. The variance at 400 m is a little low and that at depths below 2000 m is a little high; this can be attributed to different reference levels. The long term (2 October 1984 to 2 July 1985) statistics from the current meter data indicate a barotropic mode which is positively correlated (0.73) to the first baroclinic mode, giving a reference level below the zero-crossing of the first dynamical mode (1200 m).

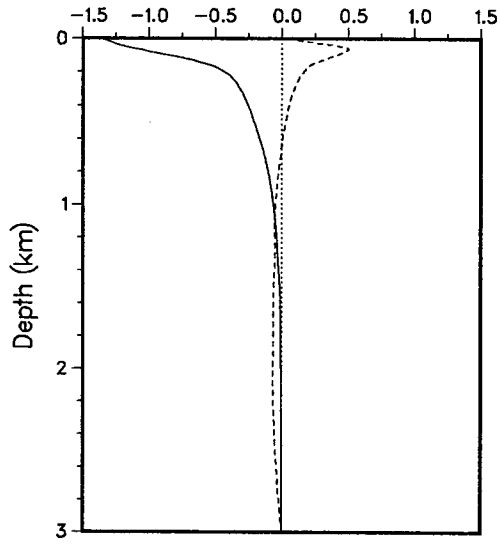

FIG. 9. Nondimensional streamfunction anomaly determined from the density eofs: solid line, eof 1; dashed line, eof 2. The streamfunction is referenced to 3000 m.

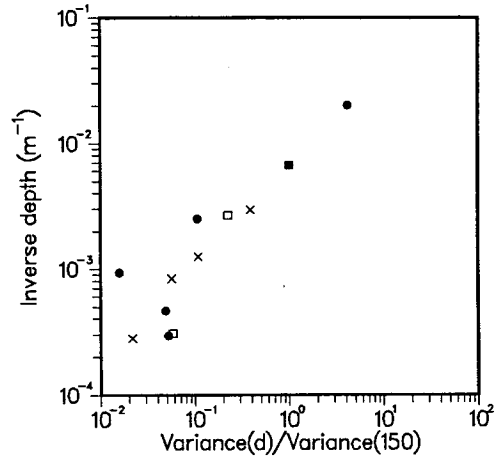

FIG. 10. Variance at depth, *d*, normalized by the variance at 150 m: ●, QG streamfunction; ×, M2 currents; □, M1 currents.

d. The estimated synoptic fields

The estimated synoptic streamfunction at 50 m, relative to 750 m, is shown for several days, starting from year day 161, the central day of OPTOMA11-AI, and including the central day of each cruise, Fig. 11a. Only the interior (130 km)^2 domain used for the model integration is shown. The evolution is essentially as noted previously for the SDH. The jet/cyclone system propagates to the west and, by day 171, the offshore extent of the jet lies outside of the domain. By day 175, the anticyclone evident in the regional SDH penetrates far into the northern part of the domain. The evolution to this state is not well-defined by the data, but there is an indication (days 167 to 173) that a smaller, weak anticyclone to the north of the jet may have played a role in either the formation of the larger feature or in interacting with the larger feature initially external to the domain: their merger could help to account for the subsequent rapid penetration of the larger feature into the OPTOMA domain. This evolution could be part of an entrainment process by which the jet, which originally (day 161) veered southward, bifurcated offshore later during the observational period. This bifurcation, inferred from available AVHRR imagery, was partially confirmed (Fig. 3b) by the DII cruise, whose sample domain was extended farther offshore to investigate the path of the jet.

Over the next ten days (177 to 187), the curvature of the jet is enhanced as the intensity of the anticyclone increases in the northwest and the cyclonic region in the southeast penetrates farther into the domain, reorienting the jet inflow on the eastern boundary. Thereafter, the anticyclone propagates westward and the cyclonic region penetrates farther into the domain until (day 215) the jet is reoriented to flow to the southwest across the entire northern portion of the domain and the cyclonic region fills the southern portion. Throughout the evolution of the streamfunction field,

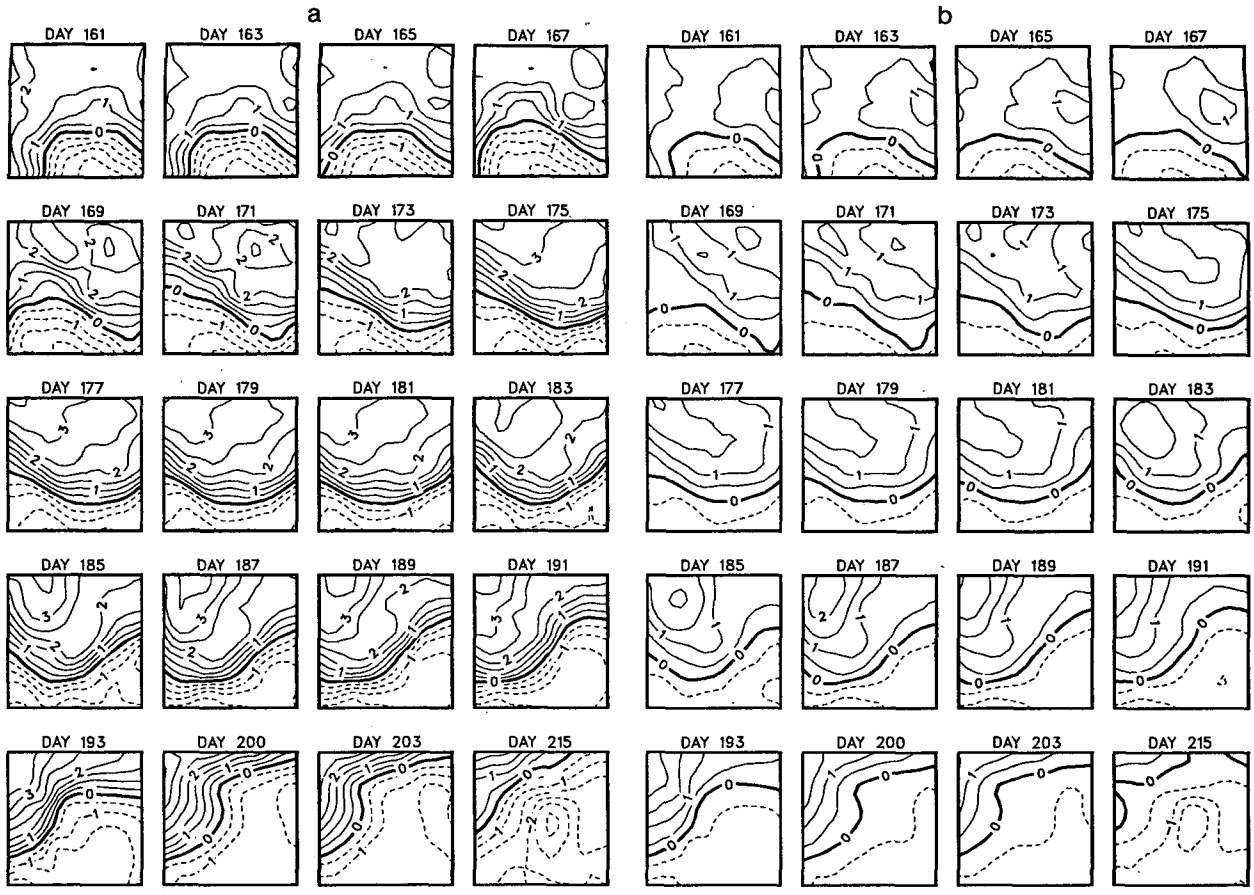

FIG. 11. The "best" OA nondimensional streamfunction, estimated by statistical space/time interpolation. Negative contours are dashed: (a) ψ (50 m). The contour interval is 0.5. (b) ψ (150 m), c.i. is 0.5. (c) ψ (2150 m), multiplied by 10; c.i. is equivalent to 0.05.

it appears that the cyclonic region comprises smaller scale, weak cyclones (diameter about 50 km or less, usually only partially evident in the primary domain, but inferred from changes in curvature in the streamfunction contours), which may decay or merely propagate offshore (e.g., days 161, 175, 191, 215). The jetlike region narrows (and intensifies) from day 161 (jet width is about 50 km, with speeds up to 50 cm s^{-1}) to 191 (jet width is about 40 km, with speeds up to 75 cm s^{-1}) and then broadens (and weakens) by day 215 (jet width at least 75 km, with speeds up to 45 cm s^{-1}).

Since most of the variance is in the first eof, the streamfunction patterns at each depth are very similar, though the amplitudes are quite different (there is an order of magnitude decrease below 150 m), Figs. 11b, c (cf. Fig. 11a), and the evolution of the streamfunction fields at deeper levels is consistent with that at 50 m. At 150 m, the current speeds are about 0.5 those at 50 m, and at 2150 m, 0.1.

4. Dynamical interpolation or hindcasts

The open-ocean, QG model presented in Haidvogel et al. (1980) and Miller et al. (1983) is used for the forecast experiments. The model evolves the QG potential vorticity, ζ, and the streamfunction, ψ, in time by integrating the vorticity equation:

$$\frac{D\zeta}{Dt} + \beta\psi_x = F,$$

where

$$\frac{D\zeta}{Dt} = \frac{\partial\zeta}{\partial t} + \alpha J(\psi, \zeta),$$

and solving the diagnostic equation (which defines the vorticity) for the streamfunction:

$$\zeta = \nabla^2\psi + \Gamma^2(\sigma\psi_z)_z, \tag{1}$$

$$\alpha = t_0\frac{V}{L}, \quad \beta = t_0\beta_0 L, \quad \Gamma^2 = \frac{f_0 L^2}{N_0^2 H^2}, \quad \sigma(z) = \frac{N_0^2}{N^2(z)}.$$

Here J is the Jacobian operator, V is a velocity scale (10 cm s^{-1}), L is a horizontal length scale of the motion (50 km), t_0 is a time scale (1.0×10^6 s), f_0 is the Coriolis parameter (0.91×10^{-4} s^{-1}), β_0 is the gradient of the Coriolis parameter (1.8×10^{-11} m^{-1} s^{-1}), N_0^2 is the stratification scale, ($N_0 = 0.011$ s^{-1}), $N^2(z)$ is the average (in space and time) stratification, and H is the scale of thermocline depth variations (150 m). For these scales, $\alpha = 2$ and $\beta = 0.9$; hence both the nonlinear and plan-

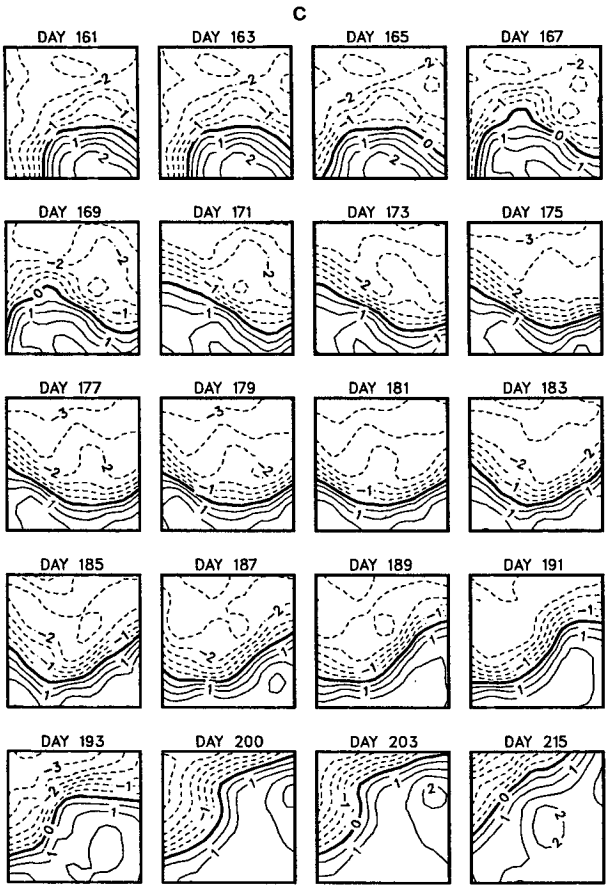

FIG. 11. (*Continued*)

etary vorticity terms are likely to be as important as local time dependence. Sub-gridscale dissipation processes are included in the vorticity equation by use of a Shapiro filter, F (e.g., see Robinson and Haidvogel, 1980).

The integration requires initial specification of streamfunction and vorticity throughout the domain (horizontal and vertical) and, at each subsequent time step, specification of streamfunction along the boundary and vorticity at inflow points along the boundary (Charney et al., 1950). In addition, the vertical velocity, w, at the top and bottom boundaries must be specified at each time step. At the surface, w is determined by the wind stress curl forcing as approximated by the largest (by at least an order of magnitude) term:

$$w = \mathbf{k} \cdot \frac{\nabla \times \tau}{\rho f},$$

where τ is the surface wind stress and $\mathbf{k}$ is the unit vector in the positive z direction. Bottom topography, $B(x, y)$, is included merely as the kinematic effect of the bottom slope (which should be no larger than $O(\epsilon)$, where ϵ is the Rossby number, $V/f_0L = 0.02$); $w = \mathbf{u} \cdot \nabla B$, where $\mathbf{u} = -\mathbf{k} \times \nabla\psi$. Nonzero vertical velocity forces density changes through the relation

$$\Gamma^2 \frac{D(\sigma\psi_z)}{Dt} = -w. \tag{2}$$

Thus, the surface and bottom values of $\sigma\psi_z$, needed for the solution of (1) for ψ, are provided by the integration in time of (2) at the surface and bottom, i.e.,

$$\sigma\psi_z = -\int_t [\Gamma^{-2} w + \mathbf{u} \cdot \nabla(\sigma\psi_z)]dt \quad \text{at} \quad z = 0, -B(x, y).$$

Bottom friction may also be included in the model. Dissipation by bottom friction is an important process in the energy balance over long time scales, but the relatively long spindown times [O(1 month) or longer], compared with forecast runs for about two weeks, associated with realistic drag coefficients, as well as the weak bottom flow in these simulations, meant that the incorporation of bottom friction had negligible effect on the forecast fields and so was neglected in the cases presented here.

In the model integration experiments finite differences are used in the vertical with the local bottom topography [slope is $O(10^{-3})$ in module 0]. The horizontal grid spacing used is 8.3 km and the time step is two hours. For all experiments, the initial and boundary data are obtained from the OA. The initial field is always the best estimate at the central day of a particular cruise, i.e., it is formed from data throughout the cruise by statistical interpolation in space–time. As described in the introduction, some dynamical experiments are hindcasts (this section) and some are forecasts (next section). For the former, the boundary data are obtained by linear interpolation between the statistically interpolated OA fields, Fig. 11. For the latter, the boundary data are obtained by statistical extrapolation from the initial state.

a. Hindcast from day 161 to 181

In the hindcast from day 161 to 181, Fig. 12, the center of the intense cyclone propagates slowly westward and its northernmost extremity gains a pronounced anticyclonic curvature which ultimately (day 175) leads to the genesis of a small (diameter about 30 km) anticyclone to the north of the jet; at this time the jet spans the width of the forecast domain. By day 177, the anticyclone has merged with a feature penetrating into the domain from the north, possibly a larger anticyclone, part of which was observed to the north of the jet during AII (days 177 and 181). The evolution of the jet and cyclone at 50 m are hindcast fairly accurately, except in the penetration of the anticyclone and curvature of the jet compared to the OA fields, Fig. 11a. The discrepancies between hindcast and analysis are probably due to the inadequacy of the boundary data which did not resolve the evolution of the anticyclone. From the model integration, this evolution did not completely conform to the simplified time dependence used in the OA. The visual agreement between the OA field and the hindcast is more marked

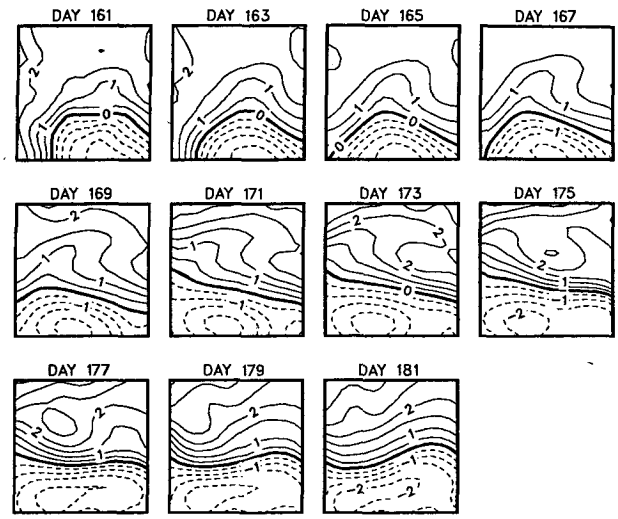

FIG. 12. Hindcast nondimensional streamfunction at 50 m (c.i. is 0.5) from an initialization at day 161. Boundary data were estimated by linear interpolation between the fields of Fig. 11.

for the streamfunction at 150 m than at 50 m (Figs. 13a and 11b); however, the error measures are comparable because of the smaller variance at depth: the NRMSD (the root-mean-square difference between the analysis and the hindcast, normalized by the standard deviation of the analysis field) for the upper three levels, calculated from interior points only, remains below 46%, and the pattern correlation is high (at least 0.95) during the model integration. Error measures for streamfunction from various hindcasts are given in Table 3 and for density in Table 4. These error measures, summarized in appendix B, are those suggested by Willmott et al. (1985) and assume that the OA fields are perfect. Possibly better statistical error measures, with confidence intervals estimated using resampling methods, are suggested by Preisendorfer and Barnett (1983); however these methods are computationally expensive if carried out for many forecast experiments.

The inclusion of the bottom slope has almost negligible effect on the hindcast fields in the upper ocean; however, even though the flow is weak in the lower ocean, the effect is marked as seen in Figs. 13b, c. From the conservation of potential vorticity, fluid flowing onshore (as at the lower levels) should acquire cyclonic vorticity. (Since onshore is oriented to the NE, there will be some balance between the bathymetric effect and the β-effect; however, the latter is smaller.) This tendency for conservation of potential vorticity is evident in Fig. 13b, and so the dynamical interpolation is probably more accurate than the OA; however, the flow is very much constrained by the imposed boundary conditions (cf. Fig. 11c). In later simulations, the inclusion of the bottom slope increases the hindcast skill—the hindcast at lower levels is in good agreement with the OA. This may indicate that the vertical extension process was more accurate for the later time period. Indeed, the deep CTDs used for the regression analysis were all from the latter half of the observational period or were external to module 0. If deep CTD casts had been available from AI, perhaps a different regression result would have been found and the OA field would have been in better agreement with the (presumably) more accurate interior forecast field.

b. Hindcast with asynoptic data

To test whether or not the synopticized estimates of the initial fields and the boundary data influence the hindcast accuracy, a model integration, similar to that above, was run with asynoptic data (the acquisition of data in module 0 took about eight days for AI and about three days for the first part of AII) assumed to coincide with day 161 and 177, Figs. 14a, b. These fields were generated in the same manner as described above except that the time dependence was omitted from the covariance function. The boundary conditions were then obtained by linear interpolation between the initial and final fields. Visually, the "asynoptic" hindcast, Fig. 14c, is not as accurate as the hindcast that used synoptic estimates for boundary data, Fig. 14d, but the error measures are similar. The "asynoptic" hindcast has a pattern correlation with the synoptic OA at 50 m of 0.96 and a NRMSD of 44% (0.96 and 39% compared with the asynoptic OA). The "synoptic" hindcast has a pattern correlation with the synoptic OA at 50 m of 0.96 and a NRMSD of 42% (Table 3). Both forecast experiments do much better than assuming that the field at day 161 persists for two weeks: the pattern correlation between the streamfunction on day 161 and that on day 177 is 0.35 and the NRMSD is 74%, at 50 m.

c. Hindcast from day 177 to day 193

The model was reinitialized at day 177 and an integration run from AII to DII (day 187) and then AIII (day 191/193).

As the jet and eddy system propagates westward, both the anticyclone in the northwest and the cyclone in the southeast intensify and penetrate farther into the domain causing a reorientation of the jet across the domain. Visually, the hindcast fields at day 187, Fig. 15, compare better with the OA fields, Fig. 11, than

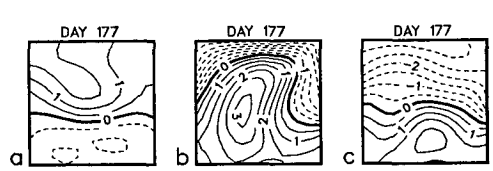

FIG. 13. Hindcast nondimensional streamfunction for day 177 from an initialization at day 161: (a) ψ (150 m), with c.i. 0.5, (b) ψ (2150 m), multiplied by 10 (c.i. equivalent to 0.05) when the effect of the local topographic slope is included and (c) ψ (2150 m) when a flat bottom is assumed.

TABLE 3. Error measures for forecast streamfunction.

Initial day	Forecast day	Correlation			NRMSD*			NRMSU*		
		50 m	150 m	2150 m	50 m	150 m	2150 m	50 m	150 m	2150 m
Flat bottom										
161	175	0.97	0.96	0.86	38	43	67	22	30	50
161	177	0.96	0.96	0.85	45	47	72	30	31	52
161	181	0.89	0.86	0.84	70	83	70	48	52	51
Local bottom slope										
161	175	0.98	0.96	0.54	35	40	140	20	29	74
161	177	0.96	0.96	0.49	42	43	150	29	30	77
161	181	0.90	0.87	0.47	67	80	146	47	52	68
Wind stress curl										
161	175	0.97	0.95	0.56	42	47	137	25	33	73
161	177	0.95	0.95	0.50	49	50	148	33	34	76
161	181	0.89	0.86	0.48	69	81	145	48	53	68
Asynoptic initialization										
161	177	0.96	0.92	0.82	39	49	79	26	35	55
Local bottom slope										
177	181	0.98	0.97	0.93	22	27	50	21	24	36
177	187	0.97	0.95	0.81	33	49	82	27	31	49
177	191	0.97	0.95	0.71	32	43	85	26	33	50
Wind stress curl										
177	181	0.98	0.97	0.93	21	27	54	21	25	37
177	187	0.98	0.93	0.80	43	62	85	32	38	48
177	191	0.93	0.86	0.72	55	72	86	36	45	48
Flat bottom										
187	191	0.99	0.98	0.93	17	22	45	15	22	34
187	200	0.86	0.86	0.84	71	68	88	65	65	60
Local bottom slope										
187	191	0.99	0.98	0.96	17	22	28	16	21	25
187	200	0.87	0.90	0.94	73	61	50	61	53	35
Wind stress curl										
187	191	0.99	0.98	0.96	17	26	28	15	22	25
187	200	0.95	0.93	0.96	45	64	37	40	48	30
Constant wind stress curl										
200	215	0.96	0.94	0.95	32	34	33	28	30	31

* Expressed as a percentage.

for the previous experiment. At day 187, the hindcast streamfunction has slightly more curvature than that in the OA. At day 193, the curvature in the hindcast field is comparable to that in the OA, but is slightly smoother. The cyclone to the south of the jet is more intense in the hindcast. The error measures in the upper ocean are comparable for the two experiments after 14 days (Tables 3 and 4); at the lower levels, the "errors" are still high in this experiment, but they are lower than for the previous experiment, indicating the increased applicability, during this period, of the vertical extension regression and so the improvement in the OA.

d. Wind stress curl forcing

In the next two hindcast experiments, it was found that wind stress curl was an important forcing mechanism and its inclusion was necessary for accurate hindcasts. The wind stress curl during the observing period, Fig. 16, was calculated from the six-hourly wind analyses from the Fleet Numerical Oceanography Center (FNOC). [These analyses are on a grid spacing of roughly 330 km at this latitude, and the wind stress curl may be underestimated by as much as 50% (Saunders, 1976).] The six-hourly values were smoothed (using running 0.25–0.5–0.25 weights) to eliminate some shorter time-scale noise to which the ocean mesoscale would not respond (and, in fact, the hindcast using the smoothed values was virtually identical to that using the raw values). The previous experiments were rerun with the surface forcing; for both experiments, there was not any marked change in the hindcast fields. During the first experiment, there was one week of consistently strong positive curl, but the curl changed sign

TABLE 4. Error measures for forecast density.

Initial day	Forecast day	Correlation			NRMSD			NRMSU		
		50 m	150 m	2150 m	50 m	150 m	2150 m	50 m	150 m	2150 m
Local bottom slope										
161	175	0.98	0.95	0.77	37	47	97	21	30	56
161	177	0.95	0.95	0.69	44	49	117	32	31	60
161	181	0.90	0.85	0.46	59	83	160	49	53	75
Wind stress curl										
161	175	0.97	0.94	0.75	42	53	102	24	33	59
161	177	0.94	0.95	0.67	51	54	121	35	34	63
161	181	0.89	0.85	0.46	61	83	161	50	54	75
Local bottom slope										
177	181	0.97	0.96	0.93	25	30	58	25	27	34
177	187	0.94	0.95	0.66	34	50	137	34	32	71
177	191	0.97	0.94	0.55	24	45	153	23	36	81
Wind stress curl										
177	181	0.97	0.96	0.93	26	30	59	25	27	36
177	187	0.93	0.93	0.58	39	61	158	38	37	81
177	191	0.94	0.82	0.42	41	68	198	32	43	100
Flat bottom										
187	191	0.98	0.98	0.93	20	22	39	16	22	31
187	200	0.85	0.91	0.84	79	56	59	65	51	53
Local bottom slope										
187	191	0.98	0.97	0.91	20	23	55	16	23	38
187	200	0.83	0.91	0.81	84	55	91	68	50	62
Wind stress curl										
187	191	0.98	0.98	0.93	20	22	39	16	22	31
187	200	0.85	0.91	0.84	79	56	59	65	51	53
Constant wind stress curl										
200	215	0.94	0.95	0.83	43	30	116	37	29	67

during the experiment and the effect on the hindcast was minor. During the second experiment, the curl again changed sign, but between days 183 and 191 there were two three-day bursts of fairly strong positive curl which produce a slight (but not marked) intensification of the cyclone in the SE.

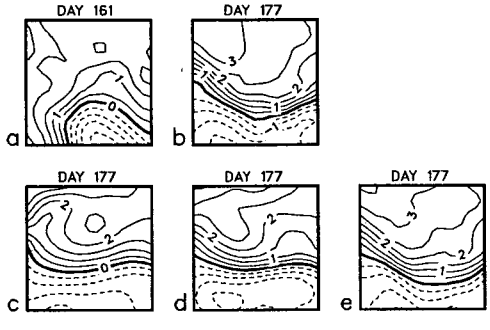

FIG. 14. Nondimensional streamfunction at 50 m (c.i. is 0.5): (a) asynoptic OA at day 161, formed by statistical interpolation in space only (i.e., ignoring time); (b) asynoptic OA at day 177; (c) hindcast using asynoptic OA for initialization and boundary data; (d) hindcast using synoptic initialization and boundary estimates; (e) OA synoptic estimate, formed by statistical space/time interpolation, at day 177.

e. Hindcast from day 187 to day 200

The model was reinitialized at day 187 and an integration run from DII to P (day 200). As mentioned above, inclusion of positive wind stress curl forcing was necessary to increase the forecast skill; during the period from DII to P, the wind stress curl was consistently positive and as high as 7×10^{-8} dyn cm^{-3}. As the anticyclone propagates offshore, the cyclonic region to the south of the jet penetrates farther into the domain, reorienting the jet across the domain. A small, weak cyclone (diameter varying between 50 to 100 km) develops, Fig. 17a.

The hindcast streamfunction at 150 m and below is in very good agreement with the OA except that the hindcast curvature change in the center of the domain is not as sharp as in the OA, Figs. 17b, c (cf. Figs. 11b, c). At 50 m, Fig. 17a, the streamfunction develops more anticyclonic curvature in the north than is evident at depth or in the OA, Fig. 11a. (Without the wind stress curl, this aspect of the hindcast is much more marked.) The jet does not change curvature across the domain. From an experiment not shown, increasing the wind stress curl improves this aspect of the streamfunction,

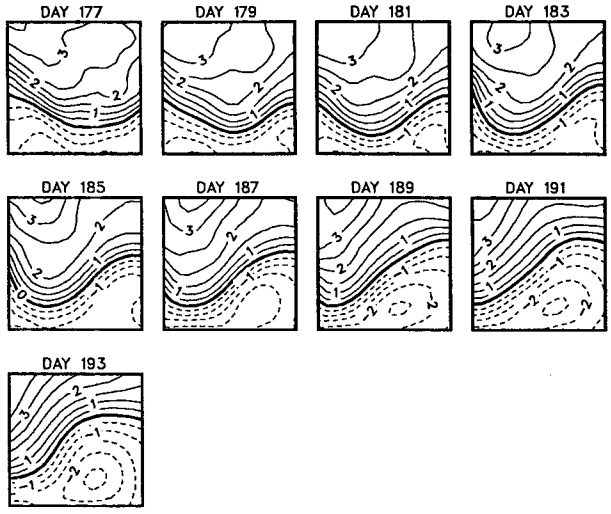

FIG. 15. Hindcast nondimensional streamfunction at 50 m (c.i. is 0.5) from an initialization at day 177. Boundary data were estimated by linear interpolation between the fields of Fig. 11.

but also increases the intensity of the cyclone to the south of the jet. The intensity is more consistent with that of day 215 than 200 and may indicate that the OA field for day 200 has underestimated the magnitude of the cyclone. This field was constructed from AXBTs to only 300 m; the vertical extension process was required over a larger portion of the water column than at other times.

f. Hindcast from day 200 to day 215

The model was reinitialized at day 200 and an integration run from P to DIII (day 215). As for the previous hindcast, without a positive wind stress curl forcing, the streamfunction in the northwest develops a much stronger anticyclonic feature than in the OA. The wind stress curl derived from FNOC analyses was much more variable during this time period than for the previous integration. The curl was negative (but small) for five days in the latter half of the integration and negligible for three days. This variation appeared to compensate for the positive curl during the initial six days and final two days of the integration: the hindcast did not differ substantially from that with no wind stress curl. Only use of a constant positive wind stress curl (for lack of justification of using an arbitrarily varying curl) improved the hindcast accuracy, Fig. 18. This is discussed further in section 9. The value of the curl, 6×10^{-8} dyn cm^{-3}, was obtained by trial and error.

The jet narrows (and intensifies, e.g., day 204) as the anticyclone appears to become more curved and smaller. By day 215, the jet has moved northward but retained its southwestward flow—the bifurcation of the flow is evident on the western boundary. The magnitude of the cyclonic region has increased and an enclosed small, weak cyclone has developed.

5. Forecast with assimilation of interior data

A pure forecast can be made by initializing the QG model with an OA field and then providing boundary data from *statistical forecasts,* i.e., the OA estimates are formed by statistical *extrapolation* in time using the time-dependent covariance function of section 3. A few days after initialization, the forecasts are limited by the inadequate knowledge of the time-dependence of the covariance function. Assimilation of interior data during the forecast period helps compensate for this inadequacy and also for physics "missing" from the dynamical model. Recently (e.g., Miller, 1986), a Kalman filter has been used to assimilate data in simplified, idealized simulations. Here, a simpler (and less expensive) approach has been taken: a linear combination of analysis fields and forecasts is formed according to

$$\psi' = \gamma\psi + (1-\gamma)\psi^*$$

where $\gamma(x, y)$ is the point error estimate of the synoptic statistical analysis, ψ^*. Although this is not an optimal combination of forecast and data fields, it represents an attempt to assimilate data during a forecast to produce a "better" forecast. After insertion of new interior data, the fields are smoothed using the Shapiro filter. The assimilation "data" are formed by objective analysis using only data within one day of the central assimilation day. In this way a truly synoptic estimate of the streamfunction at assimilation points is made and the usefulness of the data is extended horizontally according to the horizontal covariance function. The estimated OA error increases with distance from the data point. This use of OA data insertion, coupled with the filtering operation, helps ensure a smooth transition between inserted data and forecast values.

Three experiments were carried out for the period from day 177 to day 193. The first used persistent boundary data. The second, a true forecast, used boundary data estimated from AII data only, i.e., boundary data after the initialization were estimated using extrapolation in time (when necessary) by the time-dependent OA. The third experiment used the forecast boundary data of the second experiment and

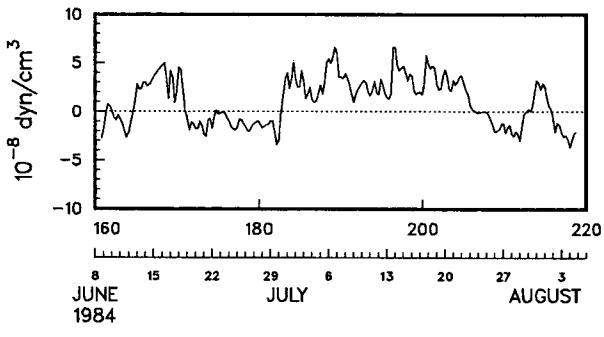

FIG. 16. Wind stress curl (in units of 10^{-8} dyn cm^{-3}) over the OPTOMA domain, estimated from FNOC wind analyses.

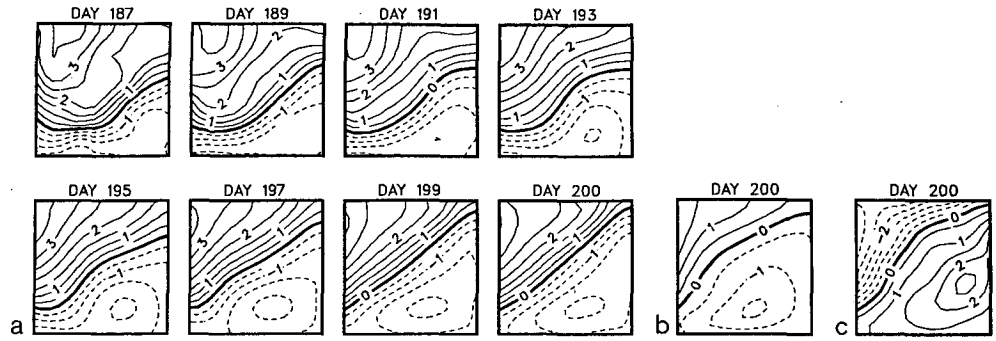

FIG. 17. Hindcast nondimensional streamfunction from an initialization at day 187, with wind stress curl forcing from FNOC included. (a) ψ (50 m) thoughout the integration (c.i. is 0.5); (b) ψ (150 m) for day 200 (c.i. is 0.5); (c) ψ (2150 m), multiplied by 10, for day 200 (c.i. is equivalent to 0.05).

assimilated synoptic data from DII, Fig. 19, from day 187 onwards.

The results of the experiments are summarized in Table 5, where each forecast is compared with the best OA estimates of Fig. 11. (Experiment 0 is the OA forecast.) The OA forecast at day 187, Fig. 20a, is quite good, with a NRMSD at 50 m of only 29%, although the anticyclone does not have the distinct north–south orientation of the "data." At day 193, the forecast OA has a much higher error but still resembles the true field in the lower half of the domain (compare Figs. 20a and 20e). Even with persistent boundary data, Fig. 20b, the model evolves the streamfunction in a consistent manner with the data: the jet axis is shifted northward resulting in an increased penetration of the cyclonic region in the south, but the reorientation of the jet from westward to southward in the center of the domain is not reproduced at day 193. Use of statistically forecast boundary data improves the visual correspondence between forecast and data, especially in the fields in the center of the domain, Fig. 20c, although at 50 m for day 193, the error measures for experiments 1 and 2 are comparable, Table 5. Whereas both these experiments overestimate the magnitude of the cyclone in the south, the forecast of Experiment 3 agrees much better with the OA (Fig. 20d, cf. Fig. 20e). At day 193, the error measures are low; the main discrepancy between the forecast and OA lies in the position of the jet curvature change, which is more to the center of the domain in the forecast. The OA error estimate at day 193 is large because of poor coverage of the domain, Fig. 2c. A comparison of Fig. 20e with the best, QG dynamically consistent estimate of the streamfunction at 50 m for day 193, Fig. 27, (as discussed in section 8) shows that the field from Experiment 3 is probably more accurate than the OA and so the error measures are inflated. With the best field estimate at 50 m used as the "perfect" data, the dynamical forecast of Experiment 2 has a correlation of 0.89, a NRMSD of 70% and NRMSU of 39%. The forecast with assimilation (Experiment 3) has a correlation of 0.96, a NRMSD of 29% and NRMSU of 22%. The improvement of forecast accuracy with data assimilation is even more marked at 150 m than at 50 m.

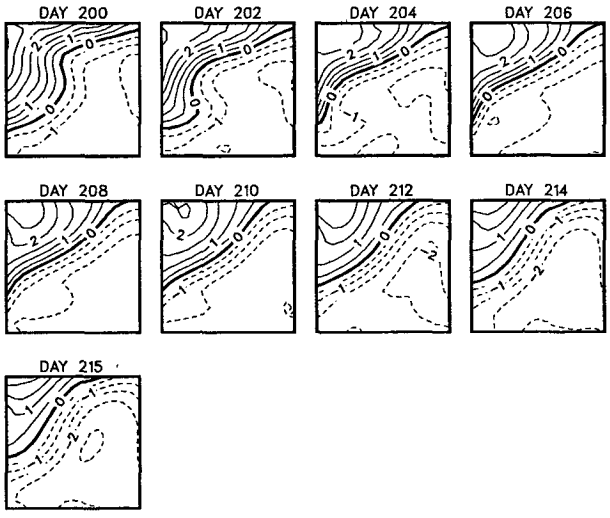

FIG. 18. Hindcast nondimensional streamfunction at 50 m (c.i. is 0.5) from an initialization at day 200. A constant wind stress curl of 6×10^{-8} dyn cm^{-3} was used.

6. Use of AVHRR data and dynamical interpolation

During the first few weeks of OPTOMA11, the SST patterns were well-correlated with the SDH patterns

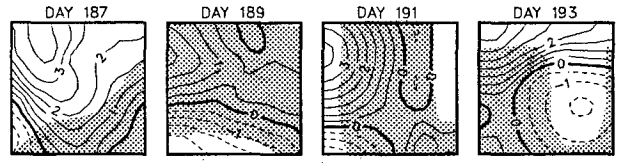

FIG. 19. OA of nondimensional streamfunction at 50 m as used for assimilation. The OA estimates were formed by statistical space–time interpolation using only data within one day of the assimilation time. Shaded regions indicate estimated OA error > 50% of the variance.

TABLE 5. Error measures for forecasts initialized at day 177.

	Day 187			Day 193		
	C*	NRMSD	NRMSU	C*	NRMSD	NRMSU
			50 m			
EXP 0	0.97	29	22	0.85	59	30
EXP 1	0.92	46	38	0.90	51	42
EXP 2	0.94	38	59	0.85	56	39
EXP 3	0.98	25	20	0.92	46	34
			150 m			
EXP 0	0.96	39	19	0.93	52	21
EXP 1	0.89	64	42	0.82	77	53
EXP 2	0.92	57	33	0.87	67	36
EXP 3	0.98	21	18	0.96	35	23

* C is the correlation at zero lag.

because of the high vertical correlation in the temperature patterns. (This is not always the case, as was shown by Rienecker et al., 1985.) When such high correlation can be identified, it is possible to infer some subsurface structure from surface fields through, e.g., an inferred relation between SST anomalies and density anomalies associated with the first density eof. The correlation between the amplitude of the first (full profile) density eof and the SST anomaly for AI, AII and DI was −0.83, yielding a regression coefficient of −0.47 sigma-*t* units/deg C. This regression coefficient was used to estimate the amplitude of the first eof from the in situ SST for the combination of AII and DI (central day approximately 179), which includes the coastal module. An upper bound, of 2.5 sigma-*t* units, was placed on the amplitude of the eof because of an apparent cutoff of its value in the cool anomaly, Fig. 21. This cutoff is probably because, even in the early stages of the experiment, the cool anomaly was partially advected offshore rather than directly related to the flow field through the thermal wind relation. The estimated pattern, Fig. 22a, agrees very well with that determined from the profile data, Fig. 22b. This same process was used with the multichannel estimate of SST (MCSST), from the NOAA-7 polar-orbiting satellite.

The MCSST fields were derived from earth-located digital AVHRR data from channels 4 (11 μm) and 5 (12 μm) which had been screened for clouds (based upon thresholds in the visible channel). The channel 4 brightness temperatures T_4 were then corrected for atmospheric contamination using NESDIS standard regression coefficients (e.g., Strong and McClain, 1984):

$$\text{MCSST} = 1.0346T_4 + 2.5779\Delta$$

where Δ is the smoothed difference $T_4 - T_5$. The smoothing operator (a moving Gaussian dome) removed noise on scales less than about 20 km. The resultant MCSST fields were used to determine satellite-derived streamfunction fields for model initialization at day 152, Fig. 23a. Subsequent boundary information was provided from MCSST fields at day 168, Fig. 23b, to give a hindcast of the field at day 161, Fig. 23c, for comparison with the in situ fields. Limited in situ data were available in the coastal module at this time, hence, the coastal data from DI were merged with the AI data, Fig. 23d. The hindcast compares well with the in situ field in the orientation and position of the jet in the domain, and in the development of the cyclones to the south of the jet. There is similar agreement with the MCSST-derived field for day 168, except that the MCSST field has a much more marked anticyclonic curvature on the north side of the jet and the southward flow in the west of the domain is more intense. The model has adjusted the estimate from the AVHRR data based on the changes of the jet inflow and outflow locations.

Dynamical interpolation (and adjustment) using this method can only be carried out for short periods be-

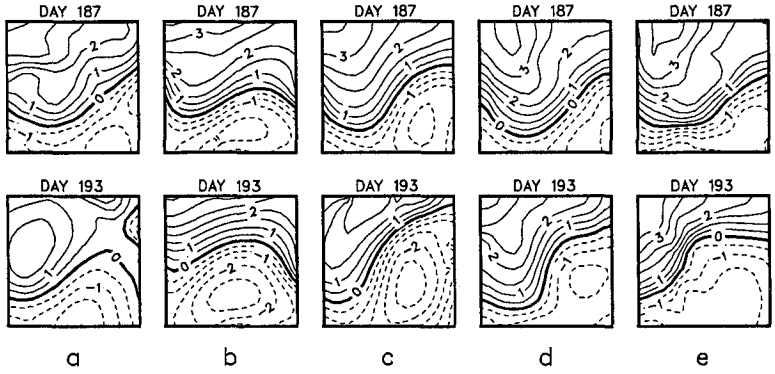

FIG. 20. Nondimensional streamfunction at 50 m from an initialization at day 177: (a) statistical forecast (i.e., statistical extrapolation from day 177 using the time-dependent covariance function of section 3); (b) dynamical forecast using persistent boundary data; (c) dynamical forecast using statistically forecast boundary data; (d) dynamical forecast, as for (c), but with assimilation of synoptic data; (e) synoptic OA estimate (i.e., statistical interpolation).

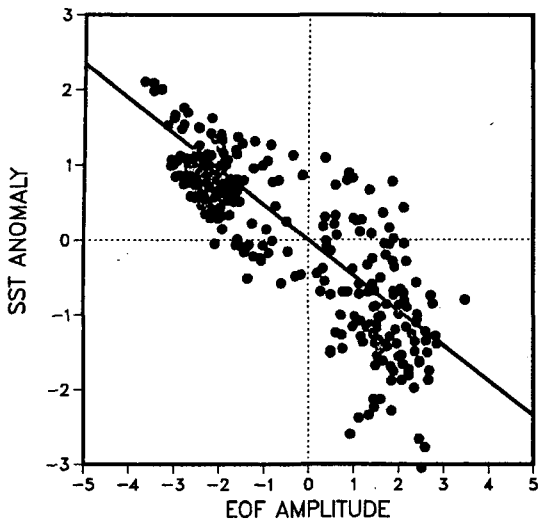

FIG. 21. In situ SST anomaly (°C) vs amplitude of first density eof (sigma-t units) from stations from AI, AII and DI. The regression line, with slope of −0.47 sigma-t units/deg C is superposed.

cause of changes in the SST due, for example, to surface heating; the mean SST, relative to which the anomaly is calculated, needs to be adjusted. In addition, of course, large areas of cloud contamination for sustained periods would preclude estimation of the required fields.

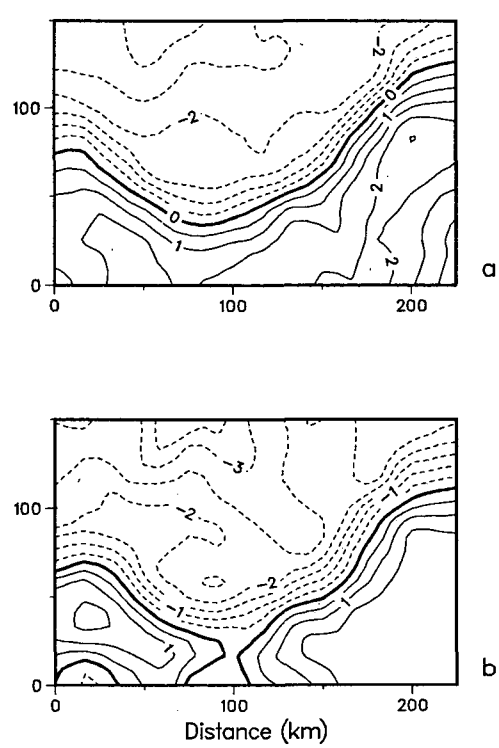

FIG. 22. Amplitude of first density eof (sigma-t units): (a) in situ; (b) estimated by regression from the in situ SST anomaly.

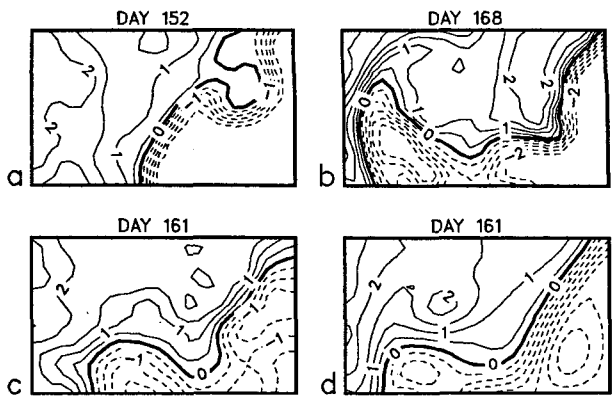

FIG. 23. Nondimensional streamfunction at 50 m (c.i. is 0.5): (a) MCSST-derived estimate for day 152, used for model initialization; (b) MCSST-derived estimate for day 168, used for estimates of boundary data; (c) in situ OA for day 161; (d) forecast for day 161.

7. Coastal module hindcasts

Under the quasi-geostrophic assumption, the influence of a topographic slope of the same order as the Rossby number is in the kinematic production of vertical velocity at the mean ocean depth. The smoothed continental slope in the coastal module, Fig. 1, has a slope of about 0.05, compared with the estimated Rossby number of 0.02. Although the continental slope is sharp, it is not so large that inclusion of coastal topography makes nonsense of the forecasts. Inclusion of the local topographic slope in QG forecasts is likely to give reasonable results if the coastal ageostrophic effects are not dominant and if the flow in the lower water column is weak, as for all cases considered here. The continental slope appears to inhibit the lower layer flow (e.g., see Stabeno and Smith, 1987).

A hindcast was carried out with an asynoptic initialization of day 161, based on the merger of data from AI and DI. The subsequent boundary data were obtained from a linear interpolation between day 161 and day 179, the fields for the latter being a merger of AII and DI. The use of the coastal data from DI in both fields means that the estimated field is essentially unchanging near the coast; this is somewhat consistent with the information obtained from the satellite data. However, the asynopticity of the fields limits the accuracy of the hindcasts. (In section 3, the asynopticity of the data in module 0 did not seriously degrade the accuracy of the forecast; however, for the extended domain used here, the field at day 161 is drawn from data acquired over 22 days, compared with only eight days for module 0.) The response to the inclusion of topography is mainly baroclinic. There is not much difference in the fields at 50 m, Figs. 24c, d; the cyclonic feature over the slope is slightly less intense, more in keeping with the verification field, Fig. 24b, and the features offshore are virtually identical. At 400 m, again, the cyclone to the south of the jet over the slope

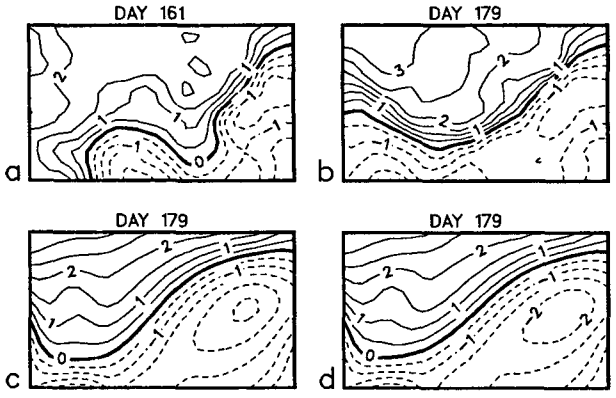

FIG. 24. Nondimensional streamfunction at 50 m (c.i. is 0.5): (a) OA for day 161, used for model initialization; (b) OA for day 179, used to estimate boundary data; (c) hindcast for day 179 when a flat bottom is assumed; (d) hindcast for day 179 when the effect of the local topographic slope is included.

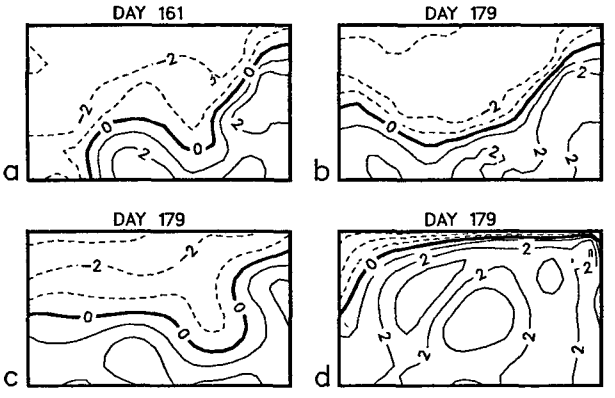

FIG. 26. As in Fig. 24 but nondimensional streamfunction at 3380 m, multiplied by 10, (c.i. is equivalent to 0.05).

is less intense when the coastal topographic slope is included, Fig. 25d; in addition, the anticyclone to the north of the jet and farther offshore is more intense and more in keeping with the verification field, Fig. 25b. At 3380 m, where there is no verification data, the response, Fig. 26d, is in keeping with conservation of potential vorticity. The flow over the slope, away from the outflow location, parallels the topography. The difference between the hindcast and the "verification field" is comparable to that in Fig. 15b.

8. Energetics of "best" field estimates

Following Robinson et al. (1986), "best" estimates of streamfunction and vorticity fields, dynamically interpolated between central cruise dates (i.e., between 161 and 177; 177 and 187; 187 and 200; 200 and 215), were formed by a linear combination of two hindcasts. The first set of fields, ψ_f, were generated by running the QG model forwards in time for T (say) days using the OA fields of Fig. 11 for initial data and boundary data interpolation. The second set of fields, ψ_b, were generated by running the model backwards in time from the final OA field (at T days) used to estimate boundary data during the generation of ψ_f. The two sets of fields were then merged:

$$\psi(t) = \frac{T-t}{T}\psi_f + \frac{t}{T}\psi_b.$$

The time series, Fig. 27, which results from such merged integration is exactly consistent with the OA fields at each cruise central day (except for day 193, which had high OA error) and the evolution intermediate between those days is dynamically (rather than statistically) constrained, except on the boundaries. Energy and vorticity analyses, as set out by Pinardi and Robinson (1986), may be performed on these fields.

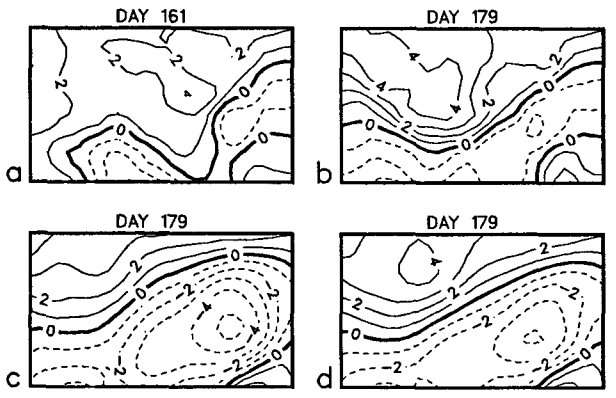

FIG. 25. As in Fig. 24 but nondimensional streamfunction at 400 m (c.i. is 0.5).

The prognostic, zero-order equations for kinetic energy (KE: $K = (u^2 + v^2)/2$) and available gravitational energy (AGE: $A = \sigma\Gamma^2(\psi_z)^2/2$) can be written

$$\frac{\partial K}{\partial t} = -\alpha\nabla\cdot(\mathbf{u}K) - \nabla\cdot\mathbf{S} - (\psi w)_z + \psi_z w + D$$

$$\frac{\partial A}{\partial t} = -\alpha\nabla\cdot(\mathbf{u}A) - \psi_z w,$$

where $\mathbf{S} = \psi\mathbf{k}\times\mathbf{u}_t + \alpha\psi\mathbf{u}\cdot\nabla(\mathbf{k}\times\mathbf{u}) - \beta y\psi\mathbf{u}$ and D is a local source/sink term associated both with the Shapiro filter and with the forecast merging process. With the terminology of Pinardi and Robinson (1986),

$$\frac{\partial K}{\partial t} = \dot{K} = \Delta F_K + \Delta F_\pi{}^t + \Delta F_\pi{}^a + \Delta F_\pi{}^\beta + \delta f_\pi - b + D$$

$$\frac{\partial A}{\partial t} = \dot{A} = \Delta F_A + b.$$

The terms on the right-hand side of the KE balance equation are, respectively, the divergence of KE flux, the divergence of pressure work through the local acceleration, the divergence of pressure work through

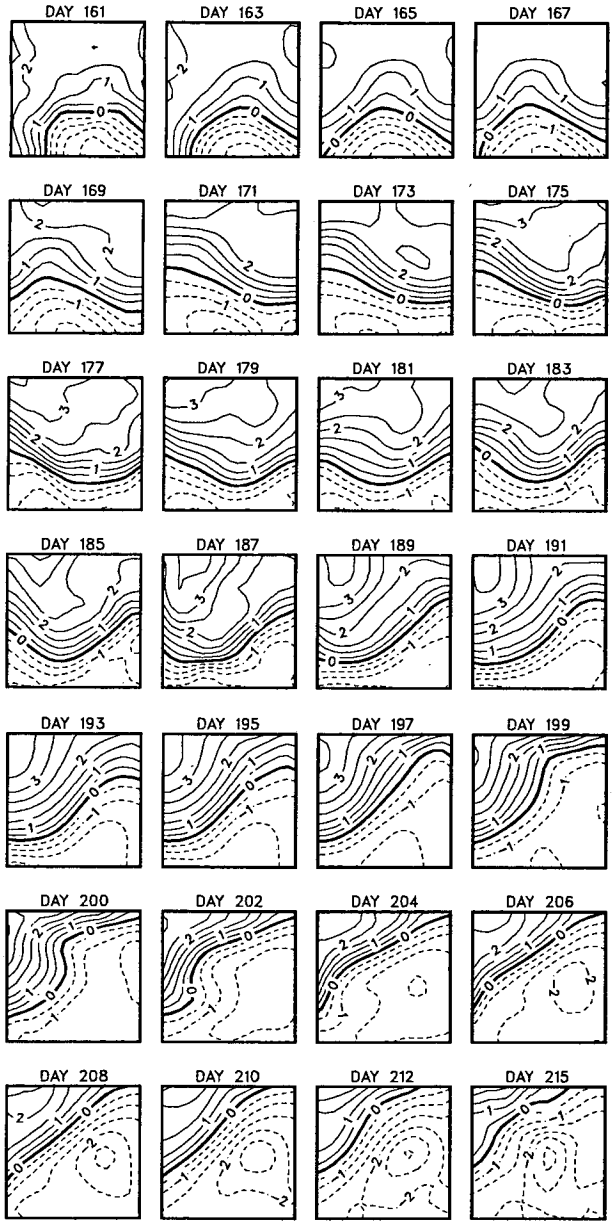

FIG. 27. Best dynamically consistent estimate of nondimensional streamfunction at 50 m.

advection, the divergence of pressure work through the planetary vorticity gradient, the divergence of pressure work in the vertical, the buoyancy work and "dissipation." The energetics analysis is carried out on the interior (100 km)^2 of the model domain.

During the phase in which the anticyclone penetrates into the north of the domain (e.g., day 173, Fig. 28), ΔF_π is important and changes sign on small scales in the north, as does δf_π. Kinetic energy increases in the jet, primarily due to ΔF_K. On the northern edge of the jet, $\Delta F_\pi + \delta f_\pi$ work to decrease the KE: as the anticyclone penetrates farther into the domain, these terms redistribute KE from the northern edge of the jet to the central part of the jet. This effect is counterbalanced primarily by D. The increase in AGE in and to the north of the jet is due equally to ΔF_A and b (Fig. 29). After the penetration of the anticyclone, the terms in the KE balance increase markedly (day 177). All terms contribute to the KE balance. In the region of maximum KE, the dominant balance involves ΔF_π, D and ΔF_K, all of which have scales of the Rossby radius of deformation (about 25 km). The Δf_π, b and $\dot{A}$ have wavelike patterns as the jet and the anticyclone undergo mutual adjustment.

The reorientation of the anticyclone to the north of the jet (e.g., day 185) is accomplished primarily through b, which decreases AGE in the northeast and increases it (with the help of ΔF_A) in the west. The buoyancy work is not important to the KE balance in which ΔF_π and D are in balance on small scales, each with wavelike structure. $\dot{K}$ is produced by $\Delta F_K - b$.

During the reorientation of the jet throughout the domain (e.g., day 199), the increase in KE along the northern boundary due to $\Delta F_K + \Delta F_\pi + \delta f_\pi$ is almost balanced by D. The increase in KE in the west of the jet is due to ΔF_K. The reorientation on the eastern boundary, which is associated with an increase in AGE, is due to b (and δf_π in the KE balance). This is probably related to the wind stress curl forcing, which was found to be important in the vorticity balance in the forecast experiments of section 4.

During the later phases, when the jet weakens slightly and the cyclone to the south of the jet intensifies, all terms (especially ΔF_π, δf_π, D and b) vary on the scale of the Rossby radius of deformation. The balance of $D + \Delta F_\pi$ works to reorient the cyclone (compare days 208, 210, 212 of Fig. 27). In a small section of the jet, KE is converted to AGE through buoyancy work; however, throughout most of the domain, AGE is converted to KE.

The importance of the wind stress curl forcing is evident in a comparison of the fields of Fig. 27 with the best estimate of the streamfunction produced as before, but without wind stress curl forcing, Fig. 30. The initial (day 200) and final (day 215) fields are constrained to be the same, but in the intermediate fields the anticyclonic curvature to the north of the jet is less developed in Fig. 27 and so does not undergo a rapid decay to the end of the period. In addition, the growth of the cyclone is smoother over the whole period rather than the rapid growth evident at day 214, Fig. 30.

The energetics for the two cases at day 208 (the central day of the forecast period and so most removed from the influence of the initial and final fields) have similar structure (Figs. 31a, b) but there are very obvious differences in sign, e.g., in b and δf_π; $\dot{K}$ and ΔF_K (not shown) are similar for the two cases. The KE is slightly larger in the jet for the wind stress curl case; the AGE is larger to the south of the jet and smaller

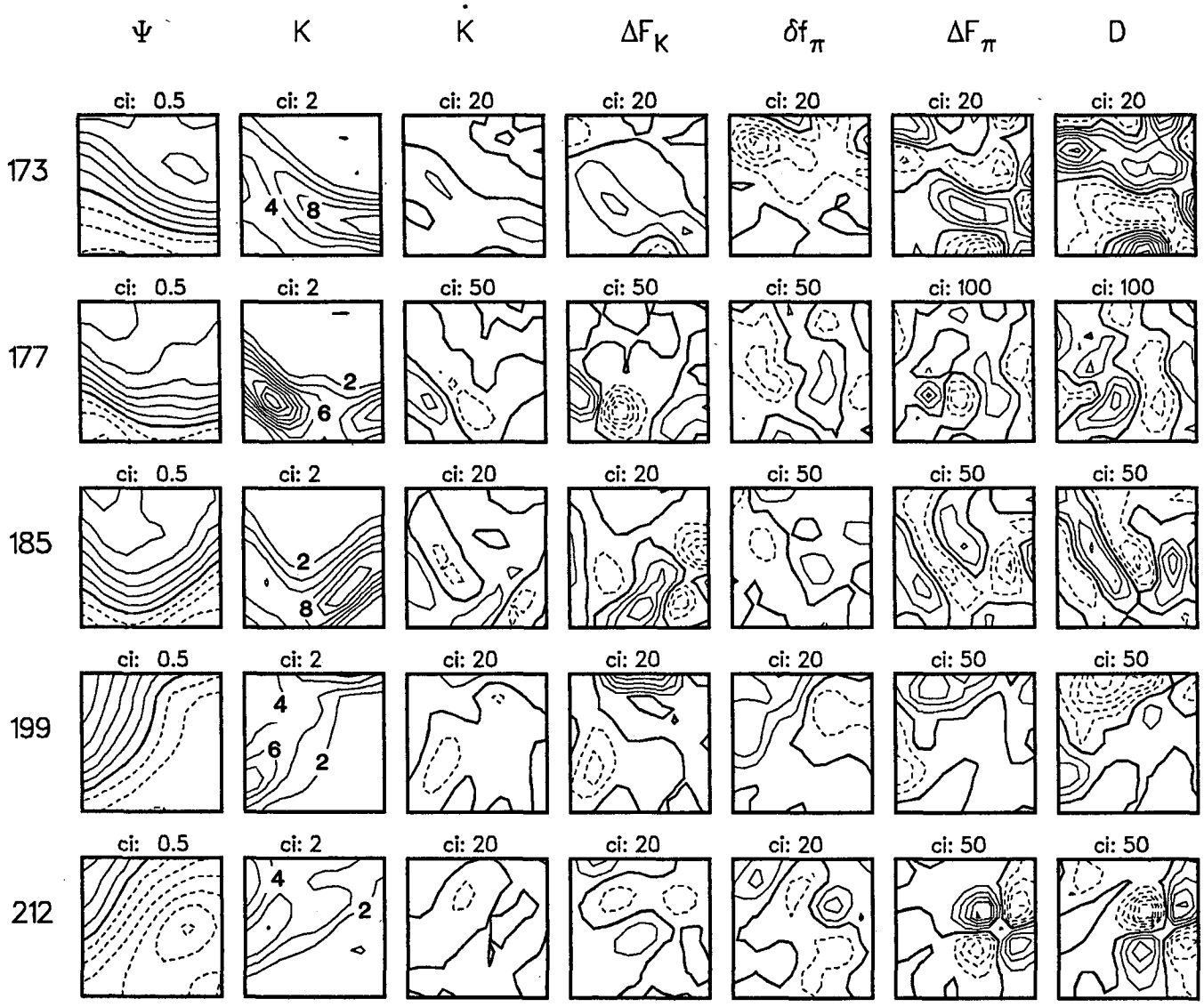

FIG. 28. Contributions to the kinetic energy balance at 50 m for selected days. Negative contours are dashed. The heavier solid line is the zero contour.

to the north than for the case with no wind stress curl. At day 212 (as the fields evolve towards the constraint of the final field) the terms in the two energy balances become more alike (Figs. 31c, d). The notable exception is the AGE balance, where, in particular, the buoyancy work term is positive over a large portion of the domain contributing to an increase in AGE when there is no curl, contrary to when the wind stress curl is included.

The energetics from the best field estimates using wind stress curl forcing have, in addition to the local conversion of AGE to KE over most of the domain, some of the baroclinic instability signatures brought to light by Pinardi and Robinson (1986), viz., growing asymmetries (in horizontal scale and amplitude) in ΔF_A, b, δf_π and $\Delta F_\pi'$, Fig. 32.

9. Summary

With the OPTOMA5 experiment it was demonstrated that the open ocean quasi-geostrophic model of Miller et al. (1983) is capable of useful dynamical interpolation to provide a time series of the evolution, between cruise periods, of features in a subdomain of the CCS. In that experiment the eddy merger, due to barotropic instability, was very different from the meandering jet and baroclinic instability encountered during OPTOMA11. In addition, wind stress curl was an important forcing mechanism during part of OPTOMA11.

OPTOMA11 was specifically designed as an ocean prediction experiment. The primary domain was sam-

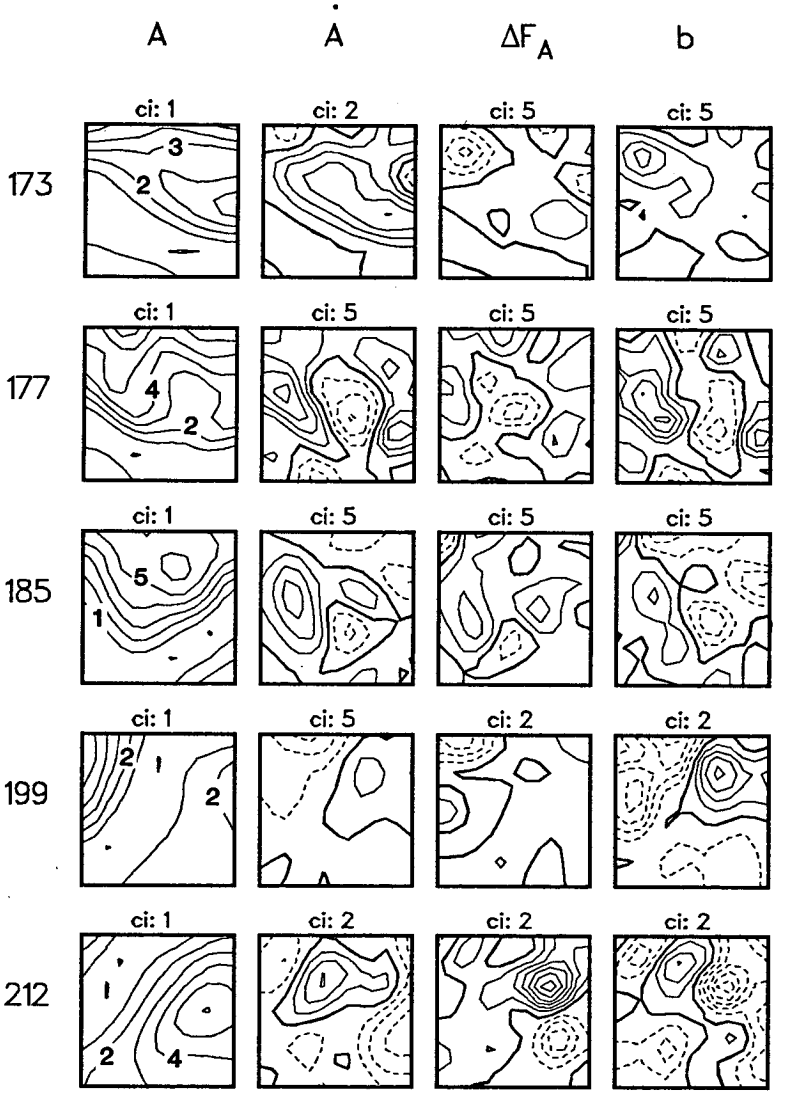

FIG. 29. Contributions to the available gravitational energy balance at 50 m for selected days.

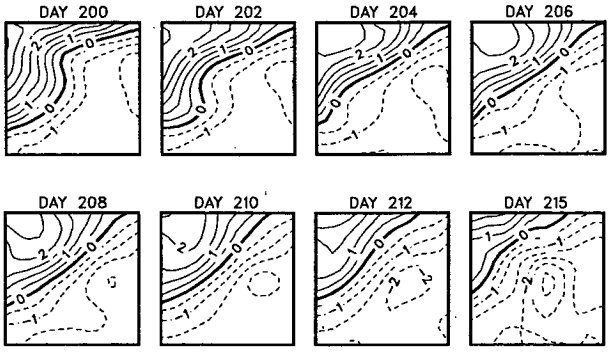

FIG. 30. Best dynamically consistent estimate of nondimensional streamfunction at 50 m when no wind stress curl forcing has been used.

pled six times over a two-month period. This allowed not only several hindcast experiments but also the estimation of a space–time covariance function which was used to make synoptic estimates of the fields and to forecast statistically boundary data for dynamical forecasts.

Since the fields were fairly slowly varying, the use of asynoptic data (collected over eight days or less) did not seriously degrade the results of hindcast experiments. This was also true for OPTOMA5 (Robinson et al., 1986) and for simulations in a larger domain in the Gulf of Mexico, by Kindle (1986) who found that spatial coverage was more important than temporal—the model adjusts the asynoptic data to a dynamically realizable field. During the initial phase of

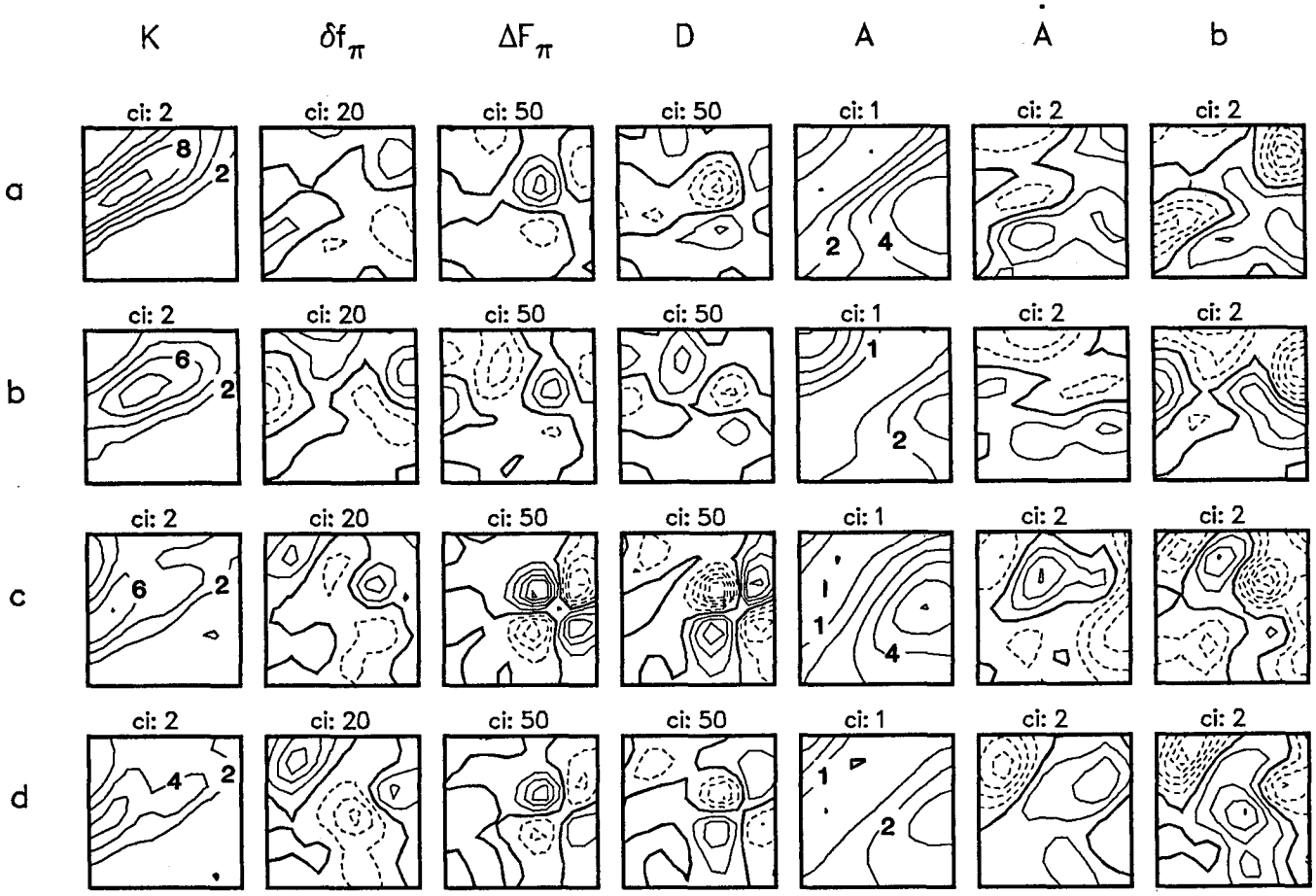

FIG. 31. Contributions to the energy balance at 50 m: (a) day 208 when wind stress curl forcing has been included; (b) day 208 when wind stress curl forcing has been omitted; (c) day 212 when wind stress curl forcing has been included; (d) day 212 when wind stress curl forcing has been omitted.

OPTOMA11, surface dynamic height (SDH) patterns were well-correlated with sea surface temperature (SST) patterns. This relationship was exploited to carry out dynamical interpolation, in an extended domain which covered the continental slope, for short periods using satellite-derived SST. Again, the model adjusted the

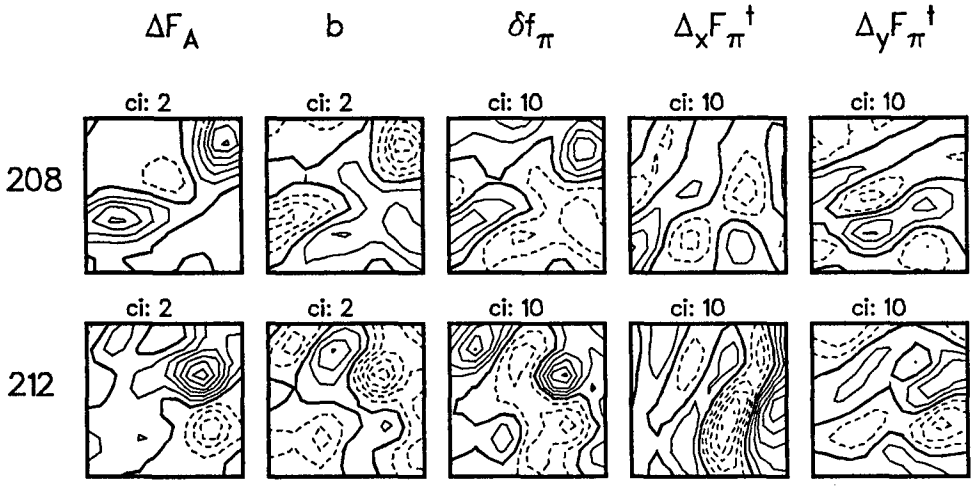

FIG. 32. Contributions to the kinetic energy balance at 50 m: $\Delta_x F_\pi^t = \partial(\psi v_t)/\partial x$; $\Delta_y F_\pi^t = \partial(\psi u_t)/\partial y$.

interior streamfunction to a dynamically realizable field, consistent with the jet inflow and outflow, but compensating for the inadequacy of the MCSST-estimated fields. Since the near-bottom flow was weak in the model integration experiments here, the inclusion of the continental slope was possible; hindcasts were improved when the local topographic slope was used instead of a flat bottom ocean.

With an appropriate time-dependent statistical model to forecast the boundary data, accurate dynamical forecasts were made; the forecasts in the interior of the domain agreed with the best estimates of the evolution of the flow field, but of course the dynamical forecast near the boundary was limited by the statistical forecast. Assimilation of synoptic data, acquired during the forecast period both in the interior and on the boundary, even by a simple merging of data and forecast compensated for the inadequacy of the statistical forecasts and increased the accuracy of the dynamical forecasts.

The QG dynamically interpolated best field estimates were used to study the energetics in a subdomain of the CCS. As for OPTOMA5, the pressure work flux,

$$\Delta F = \Delta F_\pi{}^t + \Delta F_\pi{}^a + \Delta F_\pi{}^\beta$$

was always important in the kinetic energy balance, although $\Delta F_\pi{}^\beta$ was negligible here. These terms tended to have small-scale, almost wavelike structure and were often balanced by the source/sink term associated with the filter, i.e., they were important to the transfer of energy to different scales and in the reorientation of eddy-like features. $\dot{K}$ was usually due primarily to advection (plus small imbalances between the other terms), although some localized areas of acceleration (or deceleration) in the jet itself were related to either buoyancy forcing (conversion from AGE to KE) or the convergence (or divergence) of pressure work in the vertical. Wind stress curl was an important forcing mechanism for part of the experiment. The inclusion of the wind stress curl was essential not only for an accurate forecast of the evolution of the streamfunction, but also for the interpretation of the local energetics when the cyclonic region to the south of the jet seemed to grow through baroclinic instability. With the noted importance of wind stress curl forcing comes the obvious question as to the source of reliable, relevant wind data. The FNOC analyses were adequate for most of the OPTOMA11 experiment; however, during the last phase of OPTOMA11, the assumption of a constant wind stress curl gave better results than the use of FNOC-derived values. The large grid-spacing (about 330 km) used for the FNOC analyses cannot resolve the small-scale variability [O(100 km)] evident in this region even in the long-term means calculated from observed winds (e.g., Nelson, 1977).

Overall, this paper has taken further steps in integrating models and observations to generate improved field estimates which facilitate additional analyses for investigation of dynamical processes. For example, the energetics analyses presented are illustrative of the information potentially available from a sustained effort in four-dimensional data assimilation—information which can provide a definitive understanding of how wind-driven coastal upwelling and eastern boundary current regimes operate dynamically with barotropic and baroclinic instability processes prevailing as well as Ekman pumping and suction processes.

Acknowledgments. The R/V *Acania,* the USNS *de Steiguer,* and Navy P3 flight squadrons from Moffett NAS provided invaluable support in these oceanographic surveys. The assistance of their masters and crews was exceptional, especially during sustained periods of heavy winds and seas. The success of the experiment relied on the competence and stamina of the chief scientists, Dr. Everett Carter, Mr. Leonard Walstad, Dr. Nadia Pinardi, Mr. Theodore Calhoun, Ms. Marie Colton, Ms. Arlene Bird and Prof. Christopher N. K. Mooers, and their scientific crews. The method of subprofile eofs was suggested by Dr. James Mueller. Computer time was provided by the W. R. Church Computer Center at the Naval Postgraduate School. This research was sponsored by the Physical Oceanography Program of the Office of Naval Research; their support is gratefully acknowledged.

APPENDIX A

Method of Subprofile EOFs

This method of subprofile or sectional eofs was suggested to the authors by James Mueller. It is outlined here for two sections, but the generalization to any number of sections is trivial.

Empirical orthogonal functions (eofs), which represent variance modes of the observations, are the eigenvectors of the covariance matrix:

$$\mathbf{S} = \mathbf{XX}' = \mathbf{EYY}'\mathbf{E}' = \mathbf{ED}(\lambda)\mathbf{E}'.$$

Here, $\mathbf{X}$ is the $(M \times N)$ matrix of observations, each column corresponding to a demeaned profile. There are M profiles, each with N depth points. The diagonal matrix, $\mathbf{D}(\lambda)$, contains the eigenvalues, which correspond to the variance explained by each eigenvector, $\mathbf{e}$, each of which is a column of $\mathbf{E}$. The columns of $\mathbf{Y}$ are the principal components (amplitudes of the eigenvectors) of each profile. If the number of distinct eigenvalues is Q, $< \min(M, N)$, then $\mathbf{E}$ is $M \times Q$, $\mathbf{D}$ is $Q \times Q$, and $\mathbf{Y}$ is $Q \times N$.

These relations hold for the entire profile and also for profile sections. The eigenvectors from sections and from the full profile may be interrelated through the covariance matrix:

$$\mathbf{ED}(\lambda)\mathbf{E}' = \mathbf{XX}'$$

$$= \begin{bmatrix} \mathbf{E}_1\mathbf{Y}_1 \\ \mathbf{E}_2\mathbf{Y}_2 \end{bmatrix} [(\mathbf{E}_1\mathbf{Y}_1)' | (\mathbf{E}_2\mathbf{Y}_2)']$$

$$= \begin{bmatrix} \mathbf{E}_1\mathbf{D}(\lambda_1)\mathbf{E}_1' & \mathbf{E}_1\mathbf{Y}_1\mathbf{Y}_2'\mathbf{E}_2' \\ \mathbf{E}_2\mathbf{Y}_2\mathbf{Y}_1'\mathbf{E}_1' & \mathbf{E}_2\mathbf{D}(\lambda_2)\mathbf{E}_2' \end{bmatrix}$$

where the subscript denotes the section.

Some simple matrix algebra leads to the relation, for any profile, for the estimate of the profile in section 2 from that in section 1:

$$\mathbf{x}_2 = \mathbf{E}_2\mathbf{E}_2'\mathbf{E}_1^{*}(\mathbf{E}_1^{*\prime}\,\mathbf{E}_1\mathbf{E}_1'\mathbf{E}_1^{*})^{-1}\mathbf{E}_1^{*\prime}\mathbf{x}_1$$

$$= \mathbf{A}\mathbf{x}_1$$

$\mathbf{x}_2$ is $M_2 \times 1$; $\mathbf{E}_2$ is $M_2 \times q_2$; $\mathbf{E}_2^{*}$ is $M_2 \times q$; $\mathbf{E}_1$ is $M_1 \times q_1$; $\mathbf{E}_1^{*}$ is $M_1 \times q$; where $q_2 \leqslant Q_2$; $q_1 \leqslant Q_1$; $q \leqslant Q$; and $\mathbf{E}_1^{*}$ is formed from the rows of the full-profile eigenvectors which correspond to section i. If the matrices are full-rank, then all eigenvectors, even those identified as noise, are used; this presents no problem for those profiles used in the eof determination, but for other profiles the noise may be artificially amplified. For OPTOMA11, the number of eofs used in each section was limited to two, and then the matrix $\mathbf{A}$ is a matrix of regression coefficients determined from the profiles used for the eof analysis.

APPENDIX B

Error Measures used to Assess Forecast Accuracy

Several error measures are used to assess the accuracy of the forecast fields, f. These statistics, as discussed by Willmott et al. (1985), use the OA field, o, as reference. In addition to the model and data means and variances, the root-mean-square difference,

$$\mathrm{RMSD} = [\langle d_i^2 \rangle]^{1/2}$$

(where $d_i = f_i - o_i$, and $\langle\ \rangle$ denotes the average over points used in the comparison) and the correlation,

$$C = \frac{\langle (f_i - \bar{f})(o_i - \bar{o}) \rangle}{[\langle (f_i - \bar{f})^2 \rangle \langle (o_i - \bar{o})^2 \rangle]^{1/2}}$$

are calculated. Because of the bias introduced by differences in the means, the root-mean-square difference is broken down into the systematic root-mean-square difference (determined by a linear least-squares regression of the forecast values on the data, giving the regression estimate, $\hat{f}$) and an unsystematic root-mean-square difference, defined by

$$\mathrm{RMSU} = \langle (f_i - \hat{f}_i)^2 \rangle^{1/2}.$$

In each case in this study, the root-mean-square difference measures is normalized by the standard deviation of the data.

REFERENCES

Bretherton, F. P., R. E. Davis and C. B. Fandry, 1976: A technique for objective analysis and design of oceanographic experiments applied to MODE-73. *Deep-Sea Res.*, **23,** 559–582.

Charney, J. G., R. Fjortoft and J. von Neumann, 1950: Numerical integration of the barotropic vorticity equation. *Tellus,* **2,** 237–254.

Clancy, R. M., 1983: The effect of observational error correlations on objective analysis of ocean thermal structure. *Deep Sea Res.,* **30,** 985–1002.

Haidvogel, D. B., A. R. Robinson and E. E. Schulman, 1980: The accuracy, efficiency and stability of three numerical models with application to open ocean problems. *J. Comput. Phys.,* **34,** 1–53.

Kelly, K. A., 1983: Swirls and plumes or application of statistical methods to satellite-derived sea surface temperatures. CODE Tech. Rep. 18, SIO Ref. No. 83-15.

Kindle, J. C., 1986: Sampling strategies and model assimilation of altimetric data for ocean monitoring and prediction. *J. Geophys. Res.,* **91,** 2418–2432.

Kosro, P. M., and A. Huyer, 1986: CTD and velocity surveys of seaward jets off Northern California, July 1981 and 1982. *J. Geophys. Res.,* **91,** 7680–7690.

McWilliams, J. C., and C. Y. Shen, 1980: Mesoscale modal coupling. *J. Phys. Oceanogr.,* **10,** 741–752.

Miller, R. N., 1986: Toward the application of the Kalman filter to regional open ocean modeling. *J. Phys. Oceanogr.,* **16,** 72–86.

——, A. R. Robinson and D. B. Haidvogel, 1983: A baroclinic quasi-geostrophic open ocean model. *J. Comput. Phys.,* **50,** 38–70.

Mooers, C. N. K., and A. R. Robinson, 1984: Turbulent jets and eddies in the California Current and inferred cross-shore transports. *Science,* **223,** 51–53.

Nelson, C. S., 1977: Wind stress and wind stress curl over the California Current. NOAA Tech. Rep. NMFS SSRF-714, U.S. Dept. of Commerce, 87 pp.

Pinardi, N., and A. R. Robinson, 1986: Quasi-geostrophic energetics of open ocean regions. *Dyn. Atmos. Oceans,* **10,** 185–221.

Preisendorfer, R. W., and T. P. Barnett, 1983: Numerical model-reality intercomparison tests using small-sample statistics. *J. Atmos. Sci.,* **40,** 1884–1896.

Rienecker, M. M., C. N. K. Mooers, D. E. Hagan and A. R. Robinson, 1985: A cool anomaly off Northern California: An investigation using IR imagery and in situ data. *J. Geophys. Res.,* **90,** 4807–4818.

——, ——, R. L. Smith and P. J. Stabeno, 1987: Mesoscale variability in current meter measurements in the California Current System off Northern California. *J. Geophys. Res.* (in press).

Robinson, A. R., 1983: Overview and summary of eddy science. *Eddies in Marine Science,* A. R. Robinson, Ed. Springer-Verlag, 3–15.

——, and D. B. Haidvogel, 1980: Dynamical forecast experiments with a barotropic open ocean model. *J. Phys. Oceanogr.,* **10,** 1909–1928.

——, and W. G. Leslie, 1985: Estimation and prediction of oceanic eddy fields. *Progress in Oceanography,* Vol. 14, Pergamon, 485–510.

——, J. A. Carton, N. Pinardi and C. N. K. Mooers, 1986: Dynamical forecasting and dynamical interpolation: An experiment in the California Current. *J. Phys. Oceanogr.,* **16,** 1561–1579.

Saunders, P. M., 1976: On the uncertainty of wind stress curl calculations. *J. Mar. Res.,* **34,** 155–160.

Stabeno, P. J., and R. L. Smith, 1987: Deep sea currents off northern California. *J. Geophys. Res.,* **91,** 755–771.

Strong, A. E., and E. P. McClain, 1984: Improved ocean surface temperatures from space—comparisons with drifting buoys. *Bull. Amer. Meteor. Soc.,* **65,** 138–142.

Willmott, C. J., S. G. Ackleson, R. E. Davis, J. J. Feddema, K. M. Klink, D. R. Legates, J. O'Donnell and C. M. Rowe, 1985: Statistics for the evaluation and comparison of models. *J. Geophys. Res.,* **90,** 8995–9005.